Study of impact demagnetization at Mars using Monte Carlo modeling and multiple altitude data.

Submitted to the Journal of Geophysical Research, Planets

Robert J. Lillis[1], Michael E. Purucker[2], Jasper S. Halekas[1], Karin L. Louzada[3,4], Sarah T. Stewart-Mukhopadhyay[3], Michael Manga[5], Herbert V. Frey[2]

[1]Space Sciences Laboratory, University of California Berkeley, 7 Gauss Way, Berkeley, CA 94720, USA

[2]Planetary Geodynamics Laboratory, NASA Goddard Space Flight Center, Greenbelt, MD 20771, USA

[3]Department of Earth and Planetary Sciences, Harvard University, 20 Oxford Street Cambridge MA 02138, USA.

[4]Netherlands Office for Science & Technology, Royal Netherlands Embassy, 4200 Linnean Ave NW, Washington, D.C. 20008, USA

[5]Department of Earth and planetary sciences, University of California Berkeley, Berkeley, CA 94720, USA

Abstract

The magnetic field signatures of large demagnetized impact basins on Mars offer a unique opportunity to study the magnetic properties of the crust and the processes of basin formation and impact shock demagnetization. We present a framework for determining the effects on such signatures due to the dominant direction, strength, thickness and vertical and horizontal coherence wavelengths of the surrounding crustal magnetization, as well as the demagnetization radius and the width of the demagnetization gradient zone caused by impact shock. By comparing model results with observed magnetic field profiles at 185 km and 400 km over the five largest apparently demagnetized impact structures, we find that: 1) The dominant lateral size of coherently magnetized regions of crust falls in the range ~325 km to 600 km. 2) The magnetic field observed over a circular demagnetized region is such that clear demagnetization signatures should only be visible in magnetic field maps at 185 km and 400 km altitude for demagnetization diameters larger than ~600 km and ~1000 km respectively. 3) Demagnetization radii can be meaningfully constrained despite relatively poor constraints on associated demagnetization gradient zone widths. 4) The ratio of demagnetization diameter to the outer topographic ring diameter is close to 0.8 for the Isidis, Hellas, Argyre and Utopia basins, suggesting that similar basin-forming and shock demagnetization processes occurred in each of these four ancient impacts. 5) If used in conjunction with impact simulations, such modeling may lead to improved constraints on peak pressure contours and impact energies for these basins.

1. Introduction

Mars today does not possess a global dynamo-driven magnetic field but, from evidence of strong crustal magnetization, such a field is almost certain to have existed in the planet's early history [Acuña et al., 1999]. The dynamo is thought to have started immediately following accretion/differentiation [Williams and Nimmo, 2000] prior to the formation of most of the planetary crust, >4.3 Ga ago. This hypothesis is consistent with recent lunar sample and meteoritic work implying that dynamos within planetesimals were common in the early solar system [Garrick-Bethel et al., 2009; Weiss et al., 2008, 2009].

Large impacts on Mars, such as those responsible for the Hellas and Argyre impact basins, alter the magnetization of the entire depth of crust over a geographic area comparable to the final size of the impact basin [Hood et al., 2003; Shahnas and Arkani-Hamed, 2007]. Excavation can remove magnetized material and shock heating causes thermal demagnetization within the basin [Mohit and Arkani-Hamed, 2004]. As the crust cools immediately following the impact, the melt sheet and any other crustal minerals heated above their Curie point can acquire a new thermoremanent magnetization (TRM) with a magnitude proportional to the strength of the local ambient magnetic field and the capability of the rock to carry thermoremanence. In addition, shock from the impact can add or remove net magnetization, depending on this local magnetic field and prior magnetization state of the crust. Unmagnetized materials can be magnetized in an external magnetic field through shock remanent magnetization (SRM) and existing magnetization can be reduced or erased if the minerals are shocked in an ambient field too weak to induce a sufficient SRM [Cisowski and Fuller, 1978, Gattacceca et al, 2009]. Brecciation and

fluid circulation can combine to produce post-impact hydrothermal systems which can lead to the acquisition by crustal rocks of chemical remanent magnetization (CRM), the strength of which is controlled primarily by oxygen fugacity and cooling speed [Grant, 1985]. It is important to note that essentially all magnetization in Martian impact structures is TRM, SRM or CRM, comprising what is commonly referred to as natural remanent magnetization (NRM). This is in contrast to the case of terrestrial impact structures where a substantial component of magnetization induced by the geomagnetic field can account for anywhere from ~5% to >90% of total magnetization [Ugalde et al., 2005]. Mars' lack of a global magnetic field, and hence induced magnetization, thus removes a substantial complication from the interpretation of impact basin magnetic signatures.

It is also important to note that short-wavelength, strong NRM within an impact structure (compared with outside the structure), as is observed for some terrestrial impact structures such as Chicxulub [Rebolledo-Vieyra, 2001] and Vredefort [Carporzen et al., 2005], results in magnetic field lows measured at high altitudes because magnetic fields from shorter-wavelength magnetization decay more rapidly than longer-wavelength magnetization. Indeed at Vredefort, magnetic lows are seen at aeromagnetic altitudes of hundreds of meters because the magnetization coherence length is as small as centimeters [Carporzen et al., 2005].

For any of the iron-bearing minerals likely responsible for Mars' remanent magnetism, shock demagnetization occurs out to larger distances from the impact point compared with thermal demagnetization [e.g. Mohit and Arkani-Hamed, 2004]. The very weak crustal magnetic fields measured at 100 km-400 km above the large impact basins Hellas and Argyre has for some time been taken as evidence that the basins were shock demagnetized and hence that the dynamo had

likely ceased before the remaining impact-heated crust in the youngest of these basins had cooled below its Curie point [e.g. Acuña et al., 1999; Arkani-Hamed, 2004]. This hypothesis was strengthened by the crustal magnetic field map at 185 km altitude from electron reflection (ER) magnetometry [Mitchell et al., 2007; Lillis et al., 2008a], which also showed that the Utopia, Isidis and North Polar impact basins (all greater than 1000 km in diameter) had similarly very weak magnetic signatures. Figure 1 shows the magnetic signatures of 4 of these basins at 185 km and 400 km in orthographic projection. Crater retention studies revealed these five basins to be the youngest of the large impact basins [Frey, 2006; 2008], while the 14 oldest basins display substantially stronger magnetic field signatures. This consistency led Lillis et al. [2008b] to conclude that a substantial, rapid decrease in Martian crustal magnetization occurred around an absolute model age of 4.1 Ga (based on the lunar-derived Martian cratering chronology of Hartmann and Neukum [2001]). They attributed the decrease to the end of the Martian dynamo (see figure 2 of Lillis et al. [2008b]). We acknowledge the possibility that the low magnetic fields measured over these 5 youngest large impact basins could be due to a much smaller coherence wavelength of magnetization inside the basins compared with the 14 oldest, conceivably due to some temporal change in the aqueous alteration environment on early Mars [e.g. Hood et al., 2010]. However we consider this possibility to be unlikely due to the inability of hydrothermal systems to cause mineral alteration at depths of more than a few kilometers (because rock permeability exponentially decreases with depth), compared with TRM and SRM which affect the entire ~50 km depth of magnetizable crust for impacts of this magnitude [Lillis et al., 2008b].

We wish to concentrate on the magnetic signatures of these five younger basins, making the assumption that they were formed in the post-dynamo era, i.e. there was no internally-generated geomagnetic field to remagnetize the post-impact crust.

Previous work on impact demagnetization at Mars [Hood et al., 2003; Mohit and Arkani-Hamed, 2004; Shahnas and Arkani-Hamed, 2007] has largely focused on estimating the radial pressure contours from the final (present-day) basin diameter using various assumptions about the relationship between the present-day crater topography, the diameter of the transient cavity formed immediately after the impact, the impact conditions, and the pressure conditions in the crust resulting from such an impact. From these comparisons, the authors placed qualitative constraints on magnetic properties of the crust, acknowledging the substantial uncertainty introduced by 1) the paucity of reliable shock demagnetization measurements of the primary candidate magnetic minerals and 2) our current lack of knowledge of the quantitative relationship between transient and final diameters for large impact basins, and hence the conditions of impact.

Given these still-existing uncertainties, in this paper, we elect to not compare orbital magnetic field data with estimated pressure contours as previous authors have done. Instead, we address a third uncertainty – the relationship between the measured magnetic field distribution above, and the crustal magnetization in and around, demagnetized impact basins - by modeling the underlying magnetization distribution statistically and calculating the resulting magnetic field magnitudes at orbital altitudes. We then quantitatively compare these calculated fields to the ER crustal magnetic field map of Lillis et al. [2008a] at 185 km and a new low-noise internal magnetic field map at 400 km (based on the lunar work of Purucker [2008]), in order to fit for

the most likely crustal magnetization distribution (and hence demagnetization pattern) within and near the giant impact basins. This multi-altitude approach will allow us to place important constraints on the characteristics of the crustal magnetization distribution. In future, it may also allow us to place meaningful constraints on parameters of the basin-forming impacts when better shock demagnetization data becomes available for likely candidate minerals. Conversely, it could possibly allow some constraints upon the magnetic properties of the remanence carriers when better impact modeling allows us to more confidently associate a set of pressure contours with a given Martian impact basin.

Of course, the demagnetization signatures of these giant basins may be far from pristine. Subsequent volcanism, smaller impacts and/or hydrothermal chemical alteration (i.e. chemical remanent magnetization) in/near the basins have undoubtedly modified the crustal magnetization to produce what exists today [e.g., Stokking and Tauxe, 1987; Ogawa and Manga, 2007; Lillis et al., 2009]. However, examination of the magnetic maps lets us estimate where other processes may have demagnetized crust in the vicinity of basins and exclude such regions so that our analysis is concentrated, insofar as possible, on the original impact demagnetization signature.

2. Data sets: crustal magnetic field magnitude at two altitudes

2.1. |B| at 185 km from electron reflectometry

We utilize two data sets for quantitative comparison with the magnetization modeling. The first is the electron reflection (ER) map of the field magnitude $|B|$, due to crustal sources only, at 185 km altitude above the martian datum, hereafter referred to as B_{185}. It is derived from pitch angle distributions of magnetically reflecting superthermal solar wind electrons [Mitchell et al., 2007; Lillis et al., 2008a]. It has a regionally-dependent detection threshold for crustal fields of ~1-4 nT, allowing us to examine the magnetic signatures of impact craters in greater detail than was previously possible. Uncertainties in B_{185} are well fitted by the following expression from Lillis et al. [2008a]:

$$\Delta B_{185} = 0.79\sqrt{B_{185}} \quad (1)$$

Figure 1a shows this map in orthographic projection for the hemisphere of Mars centered on 110°E, 8°N.

2.2. |B| at 400 km from internal-external field separation of magnetic field measurements

The second data set is an evaluation at 400 km of a spherical harmonic representation of the internal magnetic field of Mars using a correlative technique on the seven years (1999-2006) of mapping orbit magnetic field observations from Mars Global Surveyor (MGS). This internal dipole model exploits MGS's 88-orbit repeat geometry and incorporates radial and North-South vector component data from immediately adjacent passes. Field components of internal and external origin are separated using techniques developed for analysis of Lunar Prospector

magnetic field observations by Purucker [2008]. We shall refer to values from this 400 km-altitude map as B_{400}. Its main advantage over other internal magnetic field representations at 400 km is its appreciably lower level of external field contamination. Details of the technique, as well as uncertainties in the map, are provided in the appendix. Figure 1b shows B_{400} in orthographic projection for the hemisphere of Mars centered on 110°E, 8°N.

Place figure 1 here

3. Statistical modeling of impact demagnetization

In this paper, we will not attempt to uniquely constrain the three-dimensional distribution of subsurface magnetization in or around a given impact crater because such inversions suffer from inherent nonuniqueness [e.g. Blakely, 1995; Biswas, 2005] Also, orbital magnetic field signatures are dominated by wavelengths of magnetization comparable to the altitude of observation, with shorter wavelengths attenuating more with altitude and longer wavelengths causing relatively weaker signals [Blakely, 1995]. Instead we take a Monte Carlo approach, examining impact demagnetization within simulated crustal magnetization distributions with different magnetic and spectral characteristics. Figure 2 explains our methodology by example.

3.1. Fourier domain modeling of magnetization distributions

We define an initial three-dimensional simulation domain, typically a square-topped prism 48 km in vertical extent, consistent with recent estimates for the mean thickness of the magnetic crust of Mars [Arkani-Hamed, 2002; Voorhees, 2008; Langlais et al., 2004]. The lateral dimension is variable depending on necessity, but is in all cases at least four times larger than the impact basin size. For reasons of computational efficiency, the number of pixels in the lateral direction is a power of two. All pixels in the prism are given a magnetization vector with a direction parallel (or anti-parallel) to a single magnetic axis and with a magnitude randomly assigned from a Gaussian distribution of variable width, centered upon zero. Lorentzian distributions were also tried, and did not give appreciably different results. Negative magnetization in this context simply means it is anti-parallel to the assigned magnetic axis

direction, which can be adjusted and is meant to represent the direction of the paleomagnetic field which, with reversals, we assume originally magnetized the crust.

In the second step, we Fourier transform the magnetization magnitudes in the prism to frequency space, and then apply a spatial filter. This filter can in theory be anything we wish: low pass, high pass, bandpass, notch, power law etc., with all possible manner of roll-off characteristics. It can also be anisotropic, i.e. different in each of the three dimensions. It is well beyond the scope of this paper to cover all these possible sorts of distributions and their effects on orbital magnetic signatures; the parameter space is simply too vast. Instead we performed a limited examination of some of these filters and determined that Gaussian filters in wave number (i.e. spatial frequency) space resulted in demagnetization signatures that qualitatively match the observations of extremely weak fields in the central regions of basins (e.g. figure 1) somewhat better than power law distributions which by definition include long wavelength components. It is worth noting that power law distributions have reasonably well explained borehole and aeromagnetic data from terrestrial continental crust [e.g. Pilkington and Todoeschuck, 1993].

As shown in figure 2, panels a) - c), we apply these Gaussian filters separately in the vertical and horizontal dimensions, with the filters purposely centered on specific values of vertical and horizontal wave numbers corresponding to spatial wavelengths or 'coherence wavelengths' (a term we shall use repeatedly). The width of these Gaussian filters was (somewhat arbitrarily) chosen to be half of the central wave number. Narrower filters resulted in highly regular patterns that appeared physically unrealistic given our knowledge of terrestrial magnetization distributions [e.g. Maus and Dimri, 1995].

In the next step, we inverse Fourier transform the filtered 3-D frequency space distribution back to the original spatial domain. In the example in figure 2, the result is a distribution of magnetization with characteristic horizontal and vertical coherence wavelengths of 128 km and 12 km respectively, i.e. these are the typical wavelengths over which the magnetization varies in the horizontal and vertical directions. The typical coherence scale (i.e. size of a region of coherent magnetization) is approximately half of this wavelength, or 64 km in horizontal extent and 6 km in vertical extent, as shown in figure 2c. It is important to separately model vertical and horizontal magnetic coherence scales because the processes that give rise to remanent magnetization, such as the propagation of impact shock waves, the pooling of subsurface water and the cooling of impact melt sheets and magmatic sills, are generally strongly anisotropic because gravity only acts in the vertical direction.

We then simulate impact demagnetization by reducing the magnetization in an azimuthally symmetric pattern of arbitrary size, either uniformly or (if we wish) with additional structure in the vertical direction. Discussions of details of the simulated impact demagnetization are left to section 5.

3.2. Calculating magnetic fields at orbital altitudes

We calculate the resulting magnetic field at a given altitude (or set of altitudes) by summing the vector field due to each flat horizontal layer of pixels using the method of Blakely [1995]. This method assumes periodic boundary conditions in the horizontal (but not vertical) directions so that the field strength doesn't fall off near the edge of the simulation domain. The field magnitude at 100 km altitude above a 300 km-diameter circular demagnetized zone is shown in figure 2e.

Because the simulated magnetic field pattern comes from a randomly produced magnetization distribution, we do not try to fit these patterns to real magnetic field maps (e.g. figure 1). Instead, we take the circumferential average magnetic field strength as a function of radius and average this over typically 20 random magnetization simulations, as shown in figure 2f, g. These radial profiles of crustal magnetic field can then be quantitatively fit to circumferentially averaged crustal magnetic field maps of Martian impact basins at 185 km (ER) or 400 km (MAG), as discussed in section 2. Note that the particular magnetic intensity levels (in nT) shown in figure 2f are not important for this example since magnetic field scales linearly with magnetization strength. Only the relative intensity, as a function of radius, is important for this example.

Place figure 2 here

3.3. Dependence of magnetic field strength on magnetization properties

Even within the narrow context of our modeling framework, there are still 5 parameters that determine the average magnetic field magnitude $|B|_{ave}$ measured above a given magnetization distribution: 1) magnetization strength, 2) magnetization direction, 3) vertical coherence wavelength, 4) horizontal coherence wavelength and 5) altitude of observation. In addition, in trying to reproduce the observed radial magnetic profiles around large impact basins (e.g., figure 1), we will also attempt to constrain demagnetization radius and demagnetization gradient width (i.e. 'ramp-up' distance as shown in figure 2d). This is clearly too vast a parameter space to completely search for each basin. Therefore, we conducted a general examination of some of these parameters to see if any simplifying assumptions can be made before fitting to magnetic field observations. To do this, we calculated $|B|_{ave}$ as a function of various combinations of the

aforementioned parameters. The results are shown in figures 3, 4 and 5. We summarize the dependencies below:

1) Strength of magnetization. At each given altitude, and for each coherence wavelength, $|B|_{ave}$ varies linearly with magnetization strength [Blakely, 1995].
2) Total thickness of magnetized layer. At our altitudes of interest and for layer thicknesses less than or equal to 48 km [Voorhies et al., 2008], the magnetic field magnitude scales linearly with the thickness of the magnetized layer. Reasonable assumptions about heat flow and magnetic mineral carriers imply that the layer thickness is unlikely to be much higher than this value [Arkani-Hamed, 2005].
3) Direction of magnetization. Just as the field of a magnetic dipole is symmetric about the dipole axis, there is no dependence of $|B|_{ave}$ on the azimuthal angle of magnetization. However, the asymmetry of a dipolar magnetic field (twice as strong at the pole versus the equator) introduces a moderate dependence on the polar angle, though not a factor of two due to the canceling effects of adjacent regions of opposite magnetization. Horizontal magnetization resulted in ~30% weaker magnetic fields compared with vertical magnetization. This relationship is largely independent of horizontal coherence wavelength and altitude as shown in figure 3a. Figure 3b shows an example of the degree to which the magnetization polar angle affects demagnetization signatures. By assuming a polar angle of 45° in our fitting to observed magnetic field profiles (section 5), we shall thus incur an error of not more than 20%.
4) Vertical coherence wavelength. For our altitudes of concern above 185 km and for all horizontal coherence wavelengths, $|B|_{ave}$ varies linearly with vertical coherence wavelength. Fits for the power law exponent (i.e. the slope in figure 4a) give 1.018± 0.026. Figure 4b

shows no statistical difference between normalized magnetic field profiles 185 km above a 500 km diameter demagnetized crater for different vertical coherence wavelengths.

5) Observation altitude and horizontal coherence wavelength of crustal magnetization determine $|B|_{ave}$ according to the exponential formula given in chapter 11 of Blakely [1995]:

$$|B|_{ave} \sim e^{-kz} = e^{\frac{-2\pi z}{\lambda}} \quad (2)$$

where z is altitude, k is horizontal coherence wave number and λ is horizontal coherence wavelength. However, this formula only applies for a single coherence wavelength λ. Figure 5 plots the dependence of $|B|_{ave}$ on z and λ for the more realistic case of a Gaussian distribution of wave numbers around a central wave number (as shown in figure 2b) and a pre-impact root mean square (RMS) magnetization strength of 30 A/m. In this case, the dependence follows equation 2 up to altitudes slightly higher than λ, above which the longer wavelengths from the edges of the Gaussian distribution begin to dominate because they attenuate less quickly with altitude. Interestingly, the 50th and 90th percentiles of the global MAG and ER maps are consistent with a global average horizontal crustal magnetization coherence wavelength of ~1000 km, indicating that the magnetized crust on Mars is preserved coherently over truly enormous distances compared with Earth. This finding is consistent with best-fit coherence wavelengths from comparing modeled to observed magnetic profiles over impact basins and will be discussed in section 6.

Place figures 3, 4 and 5 here

Therefore, when we attempt to model impact demagnetization signatures for specific Martian basins there is no need to run separate simulations for different values of magnetization polar

angle, magnetization strength or vertical coherence wavelength. We shall henceforth assume a vertical coherence wavelength of 24 km, a pre-impact RMS magnetization strength of 10 A/m and a magnetization polar angle of 45°. These assumptions will simply mean a degeneracy (unavoidable in any case) between vertical coherence wavelength and magnetization strength, since $|B|_{ave}$ has a linear dependence on both, in addition to the maximum error of 20% due to magnetization direction.

3.4. Impact demagnetization

As mentioned in the introduction, when a large impact occurs in the absence of a global dynamo magnetic field, we expect substantial shock demagnetization. When considering post-impact fractional demagnetization as a function of radius and depth, there are two determining factors: 1) peak shock pressure contours and 2) the shock pressure versus magnetization curve for the magnetic mineral(s) present [Louzada et al., submitted].

Although crater scaling can be used to estimate the transient cavity diameter of simple (and to lesser extent, complex) craters and in turn the impact conditions (e.g., impactor size and velocity) [e.g. Melosh, 1989], the formation of large impact basins is still poorly understood. In particular, the relationship between the transient basin and observable final basin is unknown, making it difficult to apply crater scaling laws to large complex craters and basins. Often, for the sake of convenience, the transient crater diameter is taken to correspond to the inner ring scarp of an impact basin [e.g., Hood et al. 2003]. However, this is likely an overestimate and the true transient cavity diameter lies somewhere between the complex crater scaled solution and the inner ring scarp diameter. In the case of the Hellas basin, for example, the transient cavity

diameter is likely between the complex crater scaled solution of 800 km and the observed flat-floor diameter of 1300 to 1500 km [Louzada and Stewart, 2009].

Figure 6 (top row) shows the calculated peak shock pressure contours for a 3-dimensional CTH hydrocode simulation [McGlaun et al., 1990] of a 250 km-diameter spherical impactor of density 3000 kg/m^3, striking a layered Mars vertically at 9 km/s [Louzada and Stewart, 2009]. In this simulation, a transient diameter of approximately 800 km is formed. In a region approximately the size of the impactor centered below the impact point, the so-called isobaric core, the peak shock pressure is typically constant [Pierazzo et al., 1997] and in this case well above ~50 GPa. Outside of the isobaric core, the peak shock pressure decays both with distance from the impact point and to zero at the surface where there is a free-surface boundary. Therefore, the radial pressure gradient is large so that pressure decays with distance from the impact point along the surface much faster than with depth in the upper 50 km of the crust, where the magnetic minerals are likely to be located [e.g., Dunlop and Arkani-Hamed, 2005]. This is due to the curvature of the planet and interference of shock waves at the crust-mantle boundary layer [Louzada and Stewart, 2009]. At shallow depth,the pressure decays rapidly to 1-2 GPa at ~1000 km radial distance. Outside this region, the decay is much slower, with pressures >100 MPa out to >3000 km.

The density of Martian crust is reasonably well constrained [Neumann et al., 2004 and references therein] as is the shock equation of state of basalt [Sekine et al., 2008], therefore, it is possible to calculate the pressure contours for impacts into Martian materials using shock physics codes as long as the impact parameters are known. However, for basin forming events, due to the

uncertainties in the physics of late-stage collapse and ring formation, transient craters identified in hydrocode simulations for a given set of impact conditions cannot accurately predict the final size and character (multi-ringed or otherwise) of the basin. Thus, the problem from our perspective lies in the fact that, for a given Martian impact basin such as Hellas or Isidis, of which only the final depth and diameter are known, the peak pressure contours at the time of impact cannot be accurately determined at present.

Place figure 6 here

Currently, limited experimental pressure demagnetization data (static or shock) exists for magnetic minerals in the appropriate pressure range (a few GPa). An example of one such experiment is the static pressure demagnetization of pyrrhotite by Rochette et al. (2003) which results in complete demagnetization of pyrrhotite around 3 GPa (figure 7c). However, pressure demagnetization curves for each mineral are dependent on the magnetic domain size, coercivity of the magnetization, and chemistry of the individual minerals [e.g., Kletetschka et al., 2004; Bezaeva et al., in press; Louzada et al., 2010; Gilder et al., 2006], making it difficult to assign mineral specific demagnetization curves.

Furthermore, materials subjected to static and shock experiments do not undergo the same loading paths and neither experiment type can reproduce the strain rates and durations of pressure typical of a natural impact event. In addition, if kinetic processes (e.g., domain wall or dislocation movement and fracturing) are important demagnetization processes, then demagnetization results may be dependent upon experiment type (i.e. deformation mechanism).

Nonetheless, numerous experiments on the main candidate magnetic minerals on Mars (titanomagnetite, titanohematite, and pyrrhotite) indicate that low pressures of a few GPa result in a significant reduction of magnetization (e.g., Rochette et al., 2003). Identifying mineral specific indicator pressures (e.g., complete demagnetization at a certain pressure level) remains difficult at present (Louzada et al., 2010, submitted).

These current limitations lead us to avoid attempting to calculate fractional demagnetization versus radius and depth for individual impact basins and applying it to our magnetic modeling *a priori* for comparison to orbital magnetic data. Instead, we choose a simpler approach and model the impact demagnetization with two parameters: the diameter of the demagnetized region and the distance over which the remaining fractional magnetization increases linearly from 0% to 100% (or 'ramp up' distance), where the 'ramp-up' zone is symmetric about the demagnetization radius, i.e. the fractional demagnetization is always 50% at this radius (illustrated in figure 14). In the example shown in figure 2, the demagnetization diameter is 300 km and the ramp-up zone (which we call the 'demagnetization gradient width') is 50 km wide. Following the steep pressure contours shown in figure 6b, we assume no variation in magnetization with depth, i.e. cylindrically symmetric demagnetization. We recognize that this is an oversimplification of the impact demagnetization process, but given the aforementioned uncertainties in peak pressure contours for a given basin, and as this is the first attempt to quantitatively model magnetic field signatures with demagnetization patterns, we believe a simpler approach to be more illuminating.

It is hoped that, by placing constraints on these two impact demagnetization parameters (demagnetization diameter and demagnetization gradient width), we may be able to place joint

constraints on peak pressure contours and shock pressure-magnetization curves for the dominant minerals. However, before examining specific basins, it is instructive to use our impact demagnetization model to investigate the degree to which the magnetic field signatures of even completely demagnetized basins become less discernible with increasing altitude. Readers interested only in the fitting results may skip to section 5.

4. Detectability of impact demagnetization signatures at orbital altitudes:

Global magnetic field maps published by a number of authors [e.g. Cain et al., 2003; Langlais et al., 2004; Arkani-Hamed, 2001, 2002b, 2004b], based in large part on the 400 km mapping orbit data set, fail to show clear demagnetization signatures for any basins but Hellas, Utopia, Isidis and Argyre, all greater than 1100 km in diameter. The ER map at 185 km of Lillis et al. [2004, 2008a] additionally shows clear signatures over the 800 km-1200 km basins Prometheus [Kletetschka et al., 2008], Ladon [Lillis et al., 2008a] and North Polar [Lillis et al., 2008b], plus several craters as small as ~600 km, e.g. basins within Acidalia Planitia and the Margaritifer basin [Lillis et al., 2008a].

According to the catalog of Martian quasi-circular topographic depressions and circular thin-crust areas of Frey [2006, 2008], there are more than 350 craters on Mars between 300 km and 600 km in diameter. Given the assumption that the Martian dynamo ceased at or somewhat before the Utopia impact ~4.1 Ga [Lillis et al., 2008b], it is likely that a sizable fraction of the craters in this size range formed in the post-dynamo era, and should therefore leave circular demagnetized zones around the impact point. These zones should penetrate the entire thickness of the magnetic layer for basins larger than 200 km, as can be deduced from analytical radius-pressure relationships [e.g. Melosh, 1989; Arkani-Hamed, 2005], assuming that the same scaling relationships hold for large basins as for smaller impact structures.

Therefore, why do we not observe hundreds or at least many dozens of quasi-circular 'holes' in the crustal magnetic field pattern corresponding to the locations of these craters? This question

has been addressed in recent publications. Mohit and Arkani-Hamed [2004] examined magnetization maps derived by magnetic inversion from MGS MAG data by Arkani-Hamed [2002] for craters 250 km to 500 km in diameter. However, the inherent non-uniqueness of such inversions [Blakely, 1995] and the limited spatial resolution of orbital magnetic field data suggests substantial uncertainty in the inferred magnetization distributions shown in figure 5 of Mohit and Arkani-Hamed [2004] and hence the conclusion that substantial magnetization exists within many of the basins. Arkani-Hamed [2005] commented that this inferred magnetization could be of very high coercivity in certain regions, preventing a substantial fraction of magnetic crust from being demagnetized by the impact. However, it is difficult to understand how at least the transient cavity of an impact basin could not be fully demagnetized, implying complete demagnetization of the crust within the transient cavity radius for any reasonable thickness of magnetic crust (again assuming the same scaling for large impact basins as for smaller impact structures).

Similarly, Shahnas and Arkani-Hamed [2007] argued that the lack of weakening in magnetic field signatures over most impact basins (excluding Isidis, Argyre and Hellas) leads to the statement that “there is no consistent evidence for appreciable impact demagnetization of the Martian crust." This conclusion is based partly on the assumption that a demagnetized zone comparable in size to the altitude of observation should be resolved in magnetic field maps, a seemingly reasonable assumption. However, to date, no rigorous magnetization modeling has been applied to test this assumption quantitatively, something we shall explore here.

One can imagine at least two reasons why we do not observe hundreds of quasi-circular 'holes' in the crustal magnetic field pattern, including: 1) reduced size of the demagnetized zone relative to the crater size (as suggested by Shahnas and Arkani-Hamed [2007]) and 2) the masking of demagnetization signatures with increasing altitude. The former we cannot address without substantial advances in Martian giant impact simulation and shock demagnetization experiments, as discussed in section 3.4. The latter, however, can be investigated with our modeling framework explained in section 3.1.

A quick observation of figure 2 shows that, as the altitude of observation increases, the measured crustal magnetic field strength rapidly decreases and that impact demagnetization signatures become substantially less clear. A 300 km-diameter demagnetized basin becomes essentially invisible (particularly when standard deviations are taken into account) in the magnetic field signature at 400 km. Figure 7 explores more of this parameter space, showing the magnetic field magnitude at 100 km, 185 km and 400 km over demagnetized craters with diameters from 300 km to 1000 km in a crust with a horizontal coherence wavelength of 512 km (recall that figure 5 showed that the dominant coherence wavelength on Mars is certainly not smaller than this value). Figure 7 demonstrates that demagnetized areas smaller than ~500 km cannot be recognized by eye at 185 km, while only demagnetized areas greater than ~1000 km display relatively unambiguous quasi-circular features at 400 km altitude. Similar simulations were carried out using a power law distribution of modeled crustal magnetization with exponents between 1 and 4. In all cases, the large-wavelength part of the spectrum resulted in substantial magnetic field in the basin centers, i.e. less clear demagnetization signatures than those shown in figure 7. Of course, many more magnetic spectra could have been tried, e.g. power laws with

cutoffs to omit the longest wavelengths, with different roll-off characteristics, but such an exhaustive parameter search is beyond the scope of this paper.

Place figure 7 here

Though instructive, plots like figure 7 are subject to the random fluctuations inherent in our technique and so cannot be used to adequately determine these 'limits of detection' for demagnetized craters. For this purpose, we introduce a useful quantity, the ratio ($B_{<0.5R}/B_{1.5\text{-}2R}$) of magnetic field magnitude inside 0.5 radii of the circular demagnetized zone to the field magnitude between 1.5 and 2 radii. The lower this ratio, the 'clearer' the demagnetization signature on a magnetic map. Figure 8 shows how $B_{<0.5R}/B_{1.5\text{-}2R}$ changes for a range of crater sizes, coherence wavelengths and altitudes, calculated from circumferential averages over 20 pre-impact random magnetization distributions for each case. Not surprisingly, panels a)-c) show that larger demagnetized craters have clearer magnetic signatures at all altitudes. Also, the 'masking' of the demagnetization signatures increases with altitude for all crater sizes for horizontal coherence wavelengths of 256 km and 512 km, but for 1024 km the smaller craters (300, 400 km) are not easily visible at any altitude because they are comparable in size to the natural undulations in the magnetization distribution. Panels 8d and 8e show a comprehensive picture of the relationship between $B_{<0.5R}/B_{1.5\text{-}2R}$, coherence wavelength and demagnetized crater diameter at our two altitudes of observation.

It suggests that crater demagnetization signatures are clearest for coherence wavelengths comparable to the observation attitude (~200 km in figure 8d and 400-500 km in figure 8e). This is because the strongest magnetic fields are those due to wavelengths of crustal magnetization (in

the crust surrounding the basin) that are comparable to the observation attitude [ch. 11, Blakely, 1995]. In addition, although it is somewhat counterintuitive, it is more difficult to see demagnetization signatures in magnetization distributions with small coherence scales at higher altitudes because the demagnetized zone itself accounts for a large-amplitude long-wavelength signal, which dominates at such altitudes. Of course, in such cases, the crustal magnetic field amplitude at higher altitudes is so small that it would likely be dominated by external fields regardless.

Figure 8 also demonstrates that, if the dominant coherence wavelength on Mars is indeed on the order of ~1000 km as suggested by figure 5 (and figures 9-13 presented later), then relatively clear demagnetization signatures should only be visible at 185 km and 400 km for craters larger than ~600 km and ~1000 km respectively. Thus it is possible to explain the lack of significant magnetic field weakening over moderate-sized impact craters (300 km-600 km) at least partially in terms of masking of the demagnetization signature with altitude, with the remainder being presumably due to the radius of complete demagnetization being smaller than the topographic rim radius.

Please figure 8 here

5. Application of the model: constraining crustal magnetization and impact demagnetization parameters

We now apply our modeling framework to five of the clearest impact demagnetization signatures on Mars. The Isidis, Argyre, Hellas, Utopia and North Polar basins are the only large (i.e. greater than 1000 km in diameter) basins that have extremely low magnetic field in their centers (mostly < 2-4 nT at 185 km). All have moderate crustal fields at the edges of, or just outside, a substantial fraction of the circumference of their main topographic rim, strongly suggesting an impact demagnetization origin for the magnetic field signature.

5.1. Database of impact demagnetization calculations

Because these simulations are time-consuming, we elected to construct a single database of circumferentially-averaged radial magnetic field profiles (each one the average of 20 separate simulations) at 185 km and 400 km altitude. As discussed earlier, each simulation had a magnetic layer starting at 10 km depth, with thickness of 48 km, a magnetization polar angle of 45°, an RMS magnetization strength of 10 A/m, and a vertical coherence wavelength of 24 km.

In order to build up adequate statistics, 20 simulations were run for all combinations of the following ranges of parameters, comprising a total of 187,200 simulations:

1) 12 logarithmically-spaced values of horizontal coherence wavelength between 64 km and 2896 km
2) 65 evenly-spaced demagnetization radii between 400 km and 2000 km (25 km intervals).
3) 12 evenly-spaced demagnetization gradient (i.e. 'ramp-up') widths between 0 km and 1100 km.

In addition, in order to allow the for direct fitting to ER and MAG magnetic field data, the overall magnetization strength could be varied arbitrarily without the need for additional simulations (recall that magnetic field varies linearly with magnetization for good values of other parameters).

5.2. Circumferential averages of B_{185} and B_{400}

Circumferentially-averaged radial profiles were calculated by binning 0.5° x 0.5° maps of B_{185} and B_{400} into 60 km-wide concentric rings around the center of the basin (locations as calculated by Frey [2008]). Because we wish to isolate the demagnetization signature, we chose to only consider ranges of azimuth angle where the magnetic field clearly increases radially at or near the edge of the basin angular ranges, thus avoiding regions that were demagnetized before or after the basin-forming impacts (e.g. the Elysium volcanic province to the west-southwest of Utopia). These angular ranges are given in table 1 and shown in panels a, b of figures 9-13.

Because the circumferential averages are not supposed to be the mean of a number of measurements of a single quantity, but rather simply the mean of a distribution, we take their uncertainties to be simply the mean of the uncertainties in each pixel making up that average (see discussion in section 2), rather than the formal definition of uncertainty in a weighted mean (i.e. the inverse square root of the sum of the inverse squares of the individual uncertainties).
The choice of radius out to which the observed magnetic field radial profiles were fit to the predicted profiles was somewhat arbitrary, but generally corresponded closely with the position of the first local maximum of B_{185}, in order to attempt to avoid magnetic field contributions from

crust too far outside the impact demagnetization zone and therefore unconnected with the impact event (see panel c of figures 9-13).

5.3. Data-model fitting results

For each basin, the full χ^2 space (defined by the above 4 parameters) was calculated. The combinations of parameters corresponding to the minimum value of χ^2 and its 4-dimensional 1-sigma confidence interval were recorded. The results are shown in table 1 and figures 9-13.

Place table 1 here

In general, the combination of magnetic field measurements at 2 different altitudes allows the demagnetization radius, coherence wavelength and magnetization strength to be reasonably well constrained for each of the five basins, while the demagnetization gradient width is far less constrained, at least within the explored interval between 0 km and 1100 km.

Due to statistical noise in our modeling process, we shall consider the entire 4-dimensional volume within the 1-sigma confidence interval as being representative of the solution. Properties of the distributions of each of the 4 variables (i.e. width, mean) within the confidence interval (instead of the single 4-d 'pixel' where χ^2 is at its minimum) will be considered as the primary factors upon which to base interpretation. Figures 9-13, panels d), j), k), l) show histograms of these distributions.

Please figures 9-13 here, each on a separate page

5.4. Magnetization Coherence wavelength

Despite the somewhat coarse resolution of the coherence wavelength parameter (given in section 5.1), the 1-sigma confidence intervals tell a consistent story regarding the dominant coherence wavelength in the regions surrounding these basins. The 1-sigma interval mean value for each of the basins is between ~650 km and 1200 km as shown in table 1 and in panel d) of figures 9-13. The constraint on coherence wavelength for North Polar basin is based on a very narrow azimuthal slice (~60°) compared to the other basins (125°-330°, given in table 1) and so does not have the same statistical robustness, which should be kept in mind when considering the results.

Two important points need to be made regarding these model results. The first point is that we have defined coherence wavelength as being the full wavelength over which the magnetization varies within the model, whereas if we wish to think of the typical size of a single region of coherently magnetized crust, the half wavelength of magnetization is more appropriate and would therefore be ~325 km-600 km. The second point is that these values are of course only valid within the context of our modeling framework, which makes the assumption of a single dominant coherence wavelength with some Gaussian distribution around it (see figure 2b). The structure of the real Martian crust is likely to be richly complex with contributions at many coherence scales, though we cannot detect scales smaller than ~100 km with any current data [Blakely, 1995]. These fitting results will be discussed further in the next (discussion) section.

5.5. Magnetization strength

The best-fit values of the magnetization strength shown in table 1 are subject to the assumption of a magnetic layer of a total thickness of 48 km and a vertical coherence wavelength of 24 km.

Both of these parameters linearly determine the magnetic field magnitude. E.g. if the pre-impact magnetic layer for Isidis was 20 km and the vertical coherence wavelength 16 km, then the inferred RMS magnetization would be the best fit value of 1.1 A/m × (48 km/20 km) × (24 km/16 km) = 3.96 A/m. Given the substantial uncertainties involved, we do not wish to read too much into the inferred magnetizations other than to state that they appear consistent with the types of iron-bearing minerals usually postulated to account for Mars' crustal remanent magnetism [e.g. Kletetschka et al., 2000; Dunlop and Arkani-Hamed, 2005]. Best-fit magnetization values for the North Polar basin are higher than the other basins as a result of the smaller best-fit coherence wavelength.

5.6. Demagnetization radii and demagnetization gradient width

With perhaps the exception of the North Polar basin, we find relatively clear constraints on the demagnetization radius, i.e. the distance between the basin center and the radius at which the magnetization has increased to 50% of its pre-impact value (i.e. the point where pink and blue lines converge in figure 14). Multiple rings have been identified around each of the basins, complicating the interpretation of comparisons between topographic and demagnetization radii. Nonetheless, in all cases the best-fit demagnetization radius is larger than the innermost topographic ring radius, though with a large range of ratios from ~1.3 for Hellas to ~2.1 for Argyre. In contrast, the demagnetization radii are always smaller than the outermost ring with ratios quite tightly clustered around 0.8 (the lone exception again being the North Polar basin with its weaker statistical robustness). If it is the case that the magnetized crust surrounding these basins shock-demagnetizes in an approximately similar manner, this may be construed as evidence that the outermost topographic ring of a giant basin is a more reliable proxy for the

peak shock pressure contours, and hence the impact energy, compared with inner rings. This will be discussed further in the next section.

In contrast, we find that we are not able to provide more than a modest constraint on the magnetization gradient width, i.e. the distance over which the model subsurface magnetization increases from zero to its pre-impact level at the edge of the basin. Panel h) of figures 9-13 show histograms of demagnetization gradient width for all of the 'pixels' inside the 4-dimensional 1-sigma confidence interval. Smaller values of gradient width provide somewhat better fits for all five basins. Mean values within the 1-sigma interval (~450 km) are of limited use for interpretation because the interval contains values spanning the entire explored range of magnetization gradient widths from 0 to 1100 km.

Place figure 14 here

6. Discussion: constraining magnetic carriers and/or impact energies

We now consider the practical applications of the bounds we have derived on horizontal magnetization coherence wavelength and demagnetization radius for these five large impact basins. As mentioned in the introduction, all our interpretations are subject to the assumption that these basins were formed in the absence of any global magnetic field.

6.1. New constraints on horizontal magnetization coherence scale

Given that the best-fit dominant magnetic coherence wavelength ranges from 650 km to 1200 km, we consider the results of this fitting exercise to be evidence for very large coherently-magnetized regions of Martian crust, with sizes in the approximate range of 325 km to 600 km (i.e. the half wavelength of our defined coherence wavelength). This is in general agreement with evidence from the global distributions of the ER and MAG data sets (shown in figure 5) and the magneto-spectral analysis of Voorhees [2008] who concluded a global distribution of uniformly-magnetized spherical caps of typical size ~650 km best fits the global magnetic field spectrum of Mars. Thus it seems quite likely that the processes which primarily account for the magnetization of the Martian crust (probably a combination of magmatic thermoremanence and hydrothermal alteration) resulted in typically enormous regions of mostly coherent magnetization.

Lillis et al. [2009] modeled crustal magnetization in a small section of southwestern Tharsis using a checkerboard-like pattern of uniformly magnetized blocks which were then thermally demagnetized by modeled magma intrusions. Profiles of B_{185} were compared to this model and it was determined that block sizes (i.e. coherence scales) of 200 to 300 km and smaller provided the best fit to the data. However, the lack of reliable data at a second altitude (i.e. other than 185 km) meant these constraints on coherence scale were much looser than the two-altitude

constraints reported in this work. Nonetheless, it is possible that coherence scales in southwest Tharsis really are smaller because this crust (and its magnetization) may have formed later and over a more extended period of time (encompassing more putative reversals of the ancient global magnetic field) as Tharsis was built [Johnson and Phillips, 2005] compared with most of the Martian crust which likely formed early and perhaps quickly [Solomon et al., 2005].

6.2. Towards constraining large basin impact parameters with magnetic field measurements

In a recent review, Louzada et al. [submitted] argue that, in order to infer properties of the magnetic carriers in the Martian crust from orbital magnetic maps, the following is required: (i) unique pressure-demagnetization curves for a wide range of magnetic minerals, (ii) accurate estimates of peak shock pressures around impact basins and (iii) crustal magnetic field maps of adequate resolution over impact structures.

As mentioned in section 3.4, different magnetic carriers display quite similar pressure-demagnetization curves which cannot be easily distinguished with current experimental techniques [Louzada et al., submitted]. In addition, the physics of late-stage basin collapse and ring formation are still quite poorly understood. In particular the relationship between the transient basin and observable final (collapsed and eroded) basin is unknown, making it very difficult to constrain peak pressure contours for specific Martian basins to better than a few GPa. These limitations, coupled with the difficulty in constraining our model demagnetization gradient width with multi-altitude magnetic field data, leads us to the conclusion that such data are very unlikely to yield meaningful constraints on the specific carriers of Martian crustal remanent magnetism, even in the event of more accurate simulations of peak pressure contours.

However, we have demonstrated in this paper that the average radius of demagnetization can be constrained (in the case of Hellas, quite narrowly) even in the absence of an effective constraint on the demagnetization gradient width. Figure 14 compares ranges of demagnetization-radius curves that match the orbital magnetic field data (i.e. fall within the 1-sigma confidence interval) for the Argyre and Hellas basins, with a depth-averaged demagnetization-radius curve calculated from CTH-simulated peak pressure contours and using the static pressure-demagnetization curve for pyrrhotite from Rochette et al. [2003].

This implies that, if we instead exploit the fact that many magnetic minerals have very similar pressure-demagnetization curves, we can use the results of many impact simulations to predict a family of demagnetization-versus-radius curves (like the orange dotted line in figure 15), each one corresponding to set of impact conditions. Within the modeling framework presented in this paper, each member of the curve family will correspond to an orbital magnetic signature, which can then be compared to circumferentially-averaged radial magnetic field profiles like those shown in panel c) of figures 9-13. This should in theory allow us to constrain impact energies and peak pressure contours for specific Martian basins and should therefore enable us to better understand the complex processes involved in the formation of large basins (i.e. multiple rings scarps etc.). This aspect will be the focus of future work.

The fact that the ratio between the outer topographic ring radius identified by Frey [2008] and the best mean demagnetization radius is very close to 0.8 for the 4 clearest large basins (Isidis, Argyre, Utopia and Hellas, see table 1) suggests that similar basin-forming mechanics and shock demagnetization processes occurred for all four impacts and also that the outer topographic ring

diameter may be a better proxy compared with inner rings for peak impact pressures. Future hydrocode simulation work should further elucidate these processes.

7. Conclusions

In this paper we have presented a framework for modeling statistically the circumferentially-averaged magnetic field signature, at orbital altitudes, of shock-demagnetized impact basins on Mars. We have investigated 7 of the factors which affect these signatures: the magnetization strength, primary direction, thickness and vertical and horizontal coherence wavelengths, as well as the demagnetization radius and the width of the demagnetization gradient (or 'ramp-up') zone caused by impact shock. We have also used magnetic field magnitude data at 2 different altitudes over 5 large apparently demagnetized (and therefore probably post-dynamo) impact structures, along with this modeling framework, in order to place constraints on the aforementioned factors. Our primary conclusions are:

1) The dominant lateral coherence wavelength of Martian crustal magnetization in the vicinity of these 5 large impact basins (and likely globally), as we have defined it, is in the range of ~650 km to 1200 km. This corresponds to typically enormous regions of coherently magnetized crust in the size range of ~350 km to 600 km. Table 1 and figures 6 and 9-13 display this effect.

2) The magnetic field observed over a circular demagnetized region depends in a complex and somewhat nonintuitive manner on the relationship between the size of the region, the coherence wavelength of the pre-impact magnetization and the altitude of observation. A prime consequence of this is that increasing altitude masks the demagnetization signature such that somewhat clear demagnetization signatures should only be visible in magnetic field maps at 185 km and 400 km altitude for demagnetization diameters larger than ~600 km and ~1000 km respectively. Thus it is possible to explain the lack of significant magnetic field weakening over

moderate-sized impact craters (300 km-600 km) at least partially in terms of this masking with the remainder possibly due to the radius of complete demagnetization being smaller than the topographic rim radius. Therefore, lower altitude data orbital data, such as we are expecting from the 2013 MAVEN mission (periapsis altitude: 120 km-150 km), will make available substantially more craters for magnetic analysis.

3) Using this kind of statistical modeling, along with multi-altitude magnetic field data, averaged demagnetization diameters can be constrained for these basins, even in the absence of constraints on the associated demagnetization gradient widths. The ratio of these demagnetization diameters to the outer topographic ring diameter is close to 0.8 for Isidis, Hellas, Argyre and Utopia, suggesting that similar basin-forming and shock demagnetization processes occurred in each of these four ancient impacts.

4) Even if orbital magnetic field data cannot ever meaningfully constrain magnetic mineralogy on Mars, the similarity of pressure-demagnetization curves for many magnetic minerals suggests that such data may lead, if used in conjunction with impact simulations, to improved constraints on peak shock pressure contours and impact energies for specific Martian impact basins. This will improve our understanding of the formation of such basins.

Acknowledgments:

We wish to thank an anonymous reviewer for some helpful suggestions. This work was supported by the NASA Mars Data Analysis program (grant NNX07AN94G) and Mars Fundamental Research program (grants NNX09AN18G and NNX07AQ69G).

.

Appendix: Derivation of a new internal magnetic field model of Mars based on mapping orbit observations using a correlative approach

The technique of developing a lower-noise global map of the internal magnetic field of a planet, described in detail by Purucker [2008] for Lunar Prospector observations of the lunar magnetic field, has been adapted for Mars in this work. It uses a correlative technique on the seven years (1999-2006) of mapping orbit magnetic field observations from Mars Global Surveyor (MGS). The technique is a space domain approach using three adjacent passes separated in space by less than 1 degree of longitude, hence the derived magnetic field parameters are most sensitive to common internal crustal sources. An equivalent source formulation in spherical coordinates [Dyment and Arkani-Hamed, 1998] is used, with the magnetized martian crust divided into blocks, each of which is assumed to have a magnetic dipole at its center. Using the observations of the vertical and north-south magnetic field, the magnitude of a series of horizontal dipoles located under the middle pass are calculated using a conjugate gradient, iterative approach [Purucker et al., 1996]. This provides an analytic means of continuing the data to a constant surface of 400 km above the mean Martian radius. The orbit characteristics of Lunar Prospector and MGS differ, and the basic repeat cycle of MGS is 88-orbits, in which the orbits repeat approximately weekly.

The MGS maps were made only from night side data, acquired at 0200 local time. The altitude-normalized magnetic field from the night side is used to build a model in which 99% of the 180 by 180 bins covering the Martian surface are filled. The only unfilled bins are associated with the polar gap, which extends from 87 degrees to the pole, and a few unpopulated bins between 85 and 87 degrees North latitude. The global model is then used to construct a degree 90 spherical harmonic model of the field via the Driscoll & Healy sampling theorem [Driscoll and Healy, 1994]. Terms up to about degree 51 are robust, as shown by the increase in power beginning at that degree, and so only those terms are used in evaluating the crustal magnetic field magnitude map we use in the present work, which is at a constant altitude of 400 km, hereafter referred to as B_{400}. Figure 15 demonstrates that the map of used in this work has approximately 50% lower non-crustal noise than the equivalent dipole magnetic model of Langlais et al. [2004].

The spherical harmonic solution, and a 2 degree grid evaluated using spherical harmonic degrees 1-51, can be found at http://core2.gsfc.nasa.gov/research/purucker/mars2009. The technique is described in detail in Purucker [2008].

Place figure 15 here

We derive the uncertainty in B_{400} first by expressing the magnitude of the crustal-only magnetic field, B_c, expressed in terms of the magnitudes of the external (i.e. non-crustal) field B_{ext} and the total magnetic field, B_{400} (i.e. the vector sum of B_c and B_{ext}):

$$B_c = -B_{ext}\cos\eta + \sqrt{B_{400}{}^2 - B_{ext}{}^2 \sin^2\eta}\,,$$

where η is the angle between the vectors $\underline{\boldsymbol{B}}_{\boldsymbol{ext}}$ and $\underline{\boldsymbol{B}}_{\boldsymbol{c}}$. The first component of the error in B_{400} is thus the difference in magnitudes between B_c and B_{400}, averaged over all values of η. The second component is simply the calibration error of the MGS magnetometer, ΔB_{cal} (~0.5 nT) [Acuña et al., 2001]. These two components are added in quadrature to give the total error ΔB_{400}:

$$\Delta B_{400} = \left[\Delta B_{cal}^2 + \left(B_{400} + \frac{1}{2\pi} \int_0^{2\pi} \left(B_{ext} \cos\eta - \sqrt{B_{400}{}^2 - B_{ext}{}^2 \sin^2 \eta} \right) d\eta \right)^2 \right]^{\frac{1}{2}} \quad (3)$$

We estimate the magnitude of the external fields present in the global map of ΔB_{400} to be 1.5-2.5 nT based on measurements in regions, such as parts of Tharsis, where crustal fields at 185 km are known to be <1 nT [Lillis et al., 2009]. Figure 16 plots ΔB_{400} as a function of B_{400} for three different values of B_{ext}. The functional form in equation 3 is used in the fitting procedure described in section 5.

Place figure 16 here

References

Acuña M. H. et al. (1999), Global distribution of crustal magnetization discovered by the Mars Global Surveyor MAG/ER experiment, *Science*, *284*, 790-793.

Arkani-Hamed, J. (2001). A 50-degree spherical harmonic model of the magnetic field of Mars, *J. Geophys. Res.*, 106, 23197-23208.

Arkani-Hamed, J. (2002a). Magnetization of the Martian crust, *J. Geophys. Res.*, 107, doi:10.1029/2001JE001496.

Arkani-Hamed, J. (2002b). An improved 50-degree spherical harmonic model of the magnetic field of Mars derived from both high-altitude and low-altitjude datasets, *J. Geophys. Res.*, 107, doi:10.1029/2001JE001835.

Arkani-Hamed, J. (2004a), Timing of the Martian core dynamo, *J. Geophys. Res*., *109*, E03006, doi:10.1029/2003JE002195.

Arkani-Hamed, J. (2004b), A coherent model of the crustal field of Mars, *J. Geophys. Res.*, 109, doi:10.1029/2003JE002265.

Arkani-Hamed,, J., (2005). Magnetic crust of Mars, *J. Geophys. Res.*, 110, E08005, doi:10.1029/2004JE002397.

Bezaeva, N.S., Gattacceca, J., Rochette, P., Sadykov, R.A., Trukhin, V.I., (submitted). An overview of the demagnetization of terrestrial and extraterrestrial rocks under hydrostatic pressure up to 1.2 GPa. *PEPI*.

Biswas, R. (2005), Nonuniqueness of the modeled magnetization factors used in determining paleopoles on Mars, Masters thesis, Southern Illinois University at Carbondale.

Blakely, R. J. (1995). Potential theory in gravity and magnetic applications. Cambridge

University press, Cambridge, UK

Cain J. C., Ferguson B. B. and Mozoni D. (2003), An n=90 internal potential function of the Martian crustal magnetic field, *J. Geophys. Res*., 107, DOI:10.1029/2000JE001487

Carporzen, L., S.A. Gilder, and R.J. Hart (2005), Palaeomagnetism of the Vredefort meteorite crater and implications for craters on Mars, *Nature, 435*, 198-201.

Cisowski S. M. and M. Fuller (1978), The effect of shock on the magnetism of terrestrial rocks, *J. Geophys. Res., 83*, 3441-3458.

Driscoll, J.R., and Healy, D.M. (1994), Computing Fourier transforms and convolutions on the 2-sphere, *Adv. Appl. Math.* 15 (2), 202-250.

Dunlop, D.J. and J. Arkani Hamed (2005), Magnetic minerals in the Martian crust, *J. Geophys. Res.*, *110*, E12S04, doi:10.1029/2005JE002404.

Frey, H. V. (2006), Impact constraints on, and a chronology for, major events in early Mars history, *J. Geophys. Res*., 111, E08S91, doi:10.1029/2005JE002449.

Frey, H. (2008), Ages of very large impact basins on Mars: Implications for the late heavy bombardment in the inner solar system, *Geophys. Res. Lett.*, 35, L13203, doi:10.1029/2008GL033515.

Garrick-Bethell, I., Weiss, B.P., Shuster, D.L., Buz, J. (2009). Early Lunar Magnetism. *Science* 323, 356.

Gilder, S.A., Le Goff, M., Chervin, J. C. (2006). Static stress demagnetization of single and multi-domain magnetite with implications for meteorite impacts. *High Pressure Research 26* (4), 539-547, doi:510.1080/08957950601092085.

Grant, F.S (1985) Aeromagnetics, geology and ore environments 1. Magnetite in igneous, sedimentary and metamorphic rocks: an overview, *Geoexploration* **23** , pp. 303–333.

Hartmann W. K. and Neukum G. (2001), Cratering chronology and the evolution of Mars, *Space Sci. Rev., 96,* 165-194.

Hood L. L., Richmond N. C., Pierazzo E. and Rochette P. (2003), Distribution of crustal magnetic fields on Mars: Shock effects of basin-forming impacts, *Geophys. Res. Lett., 30*, doi:10.1029/2002GL016657.

Hood L. L., K. P. Harrison, B. Langlais, R. J. Lillis, F. Poulet, D. A. Williams (2010) Magnetic Anomalies Near Apollinaris Patera And The Medusae Fossae Formation In Lucus Planum, Mars

Kletetschka, G., Wasilewski, P.J., Taylor, P.T. (2000), Mineralogy of the sources for magnetic anomalies on Mars. *Meteoritics and Planetary Science* 35, 895-899.

Kletetschka, G., Connerney, J.E.P., Ness, N.F., Acuña, M.H. (2004), Pressure effects on martian crustal magnetization near large impact basins. *MAPS* 39, 1839-1848.

Langlais, B., Purucker, M. E., Mandea, M., (2004), Crustal magnetic field of Mars, *J. Geophys. Res.*, doi:10.1029/2003JE002048.

Lillis, R. J., Mitchell, D. L., Lin, R. P., Connerney, J. E. P., Acuña, M. H. (2004), Mapping crustal magnetic fields at Mars using electron reflectometry, *Geophys. Res. Lett.*, **31**, L15702, doi:10.1029/2004GL020189.

Lillis, R. J., Frey, H. V., Manga, M., Mitchell, D. L., Lin, R. P., Acuña, M. H. and S. W. Bougher (2008a), An improved crustal magnetic field map of Mars from electron reflectometry: Highland volcano magmatic history and the end of the Martian dynamo, *Icarus, 194,* 575-196.

Lillis, R. J., H. V. Frey, and M. Manga (2008b), Rapid decrease in Martian crustal magnetization in the Noachian era: Implications for the dynamo and climate of early Mars, *Geophys. Res. Lett.*, 35, L14203, doi:10.1029/2008GL034338.

Lillis, R. J., J. Dufek, J. E. Bleacher, M. Manga (2009), Demagnetization of crust by magmatic intrusion near the Arsia Mons volcano: magnetic and thermal implications for the development of the Tharsis province, Mars, *J. Volcan. Geotherm. Res.*, 185, 123-138, doi:10.1016/j.jvolgeores.2008.12.007

Louzada, K.L., Stewart, S.T. (2009). Effects of Planet Curvature and Crust on the Shock Pressure Field around Impact Basins. *Geophys. Res. Lett.36*, L15203, doi:10.1029/2009GL037869.

Louzada, K.L., Stewart, S.T., Weiss, B.P., Gattacceca, J., Lillis, R.J., Halekas, J.S. (submitted). Impact demagnetization of the Martian crust: current knowledge and future directions. *Earth and Planetary Science Letters - Frontiers.*, in review, 2010.

Louzada, K. L., S. T. Stewart, B. P. Weiss, J. Gattacceca, and N. S. Bezaeva (2010). Shock and static pressure demagnetization of pyrrhotite and implications for the Martian crust. *Earth and Planetary Science Letters, 290,* p.*90-101,* doi:10.1016/j.epsl.2009.12.006.

Melosh, H. J. (1989), Impact Cratering: A Geologic Process, Oxford Univ. Press, New York.

McGlaun, J. M., S. L. Thompson, and M. G. Elrick (1990), CTH: A 3-dimensional shock-wave physics code, *Int. J. Impact Eng., 10,* 351-360, doi:10.1016/0734-743X(90)90071-3.

Mitchell, D. L., Lillis, R. J., Lin, R. P., Connerney, J. E. P., Acuña, M. H. (2007). A global map of Mars' crustal magnetic field based on electron reflectometry, *J. Geophys. Res. 112,* E1, E0100, doi 10.1029/2005JE002564

Mohit, P. S. and J. Arkani-Hamed (2004), Impact demagnetization of the Martian crust, *Icarus 168*, 305-317.

Neumann, G. A., M. T. Zuber, M. A. Wieczorek, P. J. McGovern, F. G. Lemoine, and D. E. Smith (2004), Crustal structure of Mars from gravity and topography, *J. Geophys. Res*., *109*, E08002, doi:10.1029/2004JE002262.

Ogawa, Y., and M. Manga (2007), Thermal demagnetization of Martian upper crust by magma intrusion, *Geophys. Res. Lett.*, *34*, L16302, doi:10.1029/ 2007GL030565.

Pierazzo, E., A. M. Vickery, and H. J. Melosh (1997), A Reevaluation of Impact Melt Production, *Icarus*, *127*, 408-423, doi:10.1006/icar.1997.5713.

Pilkington, M., and J.P. Todoeschuck (1993), Fractal magnetization of continental crust, *Geophys. Res. Lett.*, *20*, 627-630.

Purucker, M. E., 2008, A global model of the internal magnetic field of the Moon based on Lunar Prospector magnetometer observations, *Icarus*, *197*, 19-23.

Purucker, M., T.Sabaka, and R. Langel (1996) Conjugate gradient analysis: A new tool for studying satellite magnetic data sets, *Geophys. Res. Lett. 23*, 507-510.

Rebolledo-Vieyra, M. (2001), Magnetoestratigrafia y Paleomagnetismo del crater de impacto Chicxulub [PhD thesis]: Mexico City, National University of Mexico, 120 p.

Sekine T., Kobayashi T., Nishio M., et al. (2008), Shock equation of state of basalt, *Earth, Planets and Space, 60,* 999-1003.

Solomon, S. C. and 16 co-authors (2005), New perspectives on ancient Mars, *Science*, 307, 1214-1220

Stokking, L. B. and L. Tauxe (1987), Acquisition of chemical remanent magnetization by synthetic iron oxide**,** *Nature, 327,* 610 - 612.

Shahnas, H., and J. Arkani-Hamed (2007), Viscous and impact demagnetization of Martian crust, *J. Geophys. Res*., *112*, E02009, doi:10.1029/2005JE002424.

Smith, D. E., et al. (2001), Mars Orbiter Laser Altimeter: Experiment summary after the first year of global mapping of Mars, *J. Geophys. Res.*, 106, 23,689– 23,722.

Ugalde, H. A., Artemieva N. and Milkereit, B. (2005), Magnetization on impact structures-Constraints from numerical modeling and Petra physics in Kenkmann, T., Horz, F. and Deutsch, A., eds., Large meteorite impacts III: Geological Society of America Special Paper 384, p. 25-42

Voorhies, C. V. (2008), Thickness of the magnetic crust of Mars, J. Geophys. Res., 113, E04004, doi:10.1029/2007JE002928.

Williams, J. P., Nimmo, F. (2004), Thermal evolution of the Martian core: Implications for an early dynamo, *Geology, 32*, 97-100.

Weiss, B. P., L. E. Fong, H. Vali, E. A. Lima, and F. J. Baudenbacher (2008), Paleointensity of the ancient Martian magnetic field, *Geophys. Res. Lett.*, 35, L23207, doi:10.1029/2008GL035585.

Weiss, B.P., Carporzen, L., Elkins-Tanton, L.T., Ebel, D.S. (2009), Evidence for Internally Generated Magnetic Fields on the CV Chondrite Parent Planetesimal. *Lunar and Planetary Institute Science Conference Abstracts* 40, 2237.

Figure captions

Figure 1: Orthographic maps of the crustal magnetic field magnitude at a) 185 km and b) 400 km altitude used in this study (denoted B_{185} and B_{400}; note logarithmic scale) overlaid on shaded MOLA topography [Smith et al., 2001]. The B_{185} map was adapted from Lillis et al. [2008a]. B_{400} is taken from a new low-noise internal magnetic field model of Mars closely following the lunar work of co-author Purucker [2008] (see appendix). Impact basins >1000 km in diameter are shown as solid circles [Frey, 2008]. Each ring in multi-ringed basins is shown. Demagnetized and magnetized basins are identified with blue and red lettering, respectively. The letters are abbreviations for the following basins: Hellas (He) , Scopolus (Sc) , Isidis (Is) , Utopia (Ut), North Polar (NP), Amenthes (Am), Zephyria (Ze), Southeast Elysium (SE), Amazonis (Az).

Figure 2: Example of statistical Fourier domain modeling of impact demagnetization. Panel a) shows a 48 x 256 x 256-element random magnetization distribution where each voxel's value is drawn from a zero-centered Gaussian distribution with a standard deviation of 10 A/m. Vertical and horizontal resolution is 1 km and 4 km respectively. Panel b) shows Gaussian horizontal and vertical filters of 128 km and 12 km in the wave number domain, which are applied to the Fourier transform of the random distribution from panel a). Panel c) shows the inverse Fourier transform of the filtered wave number domain distribution, i.e. a 'real space' magnetization distribution with horizontal and vertical coherence wavelength distributions centered on 128 km and 12 km respectively. Panel d) shows the same magnetization distribution, but with a 300 km-diameter cylinder of zero magnetization, with a circumferentially and vertically uniform 50 km-wide radial 'ramp-up' zone at its edge (i.e. magnetization increases linearly from 125 km to 175

km radius). Panel e) shows the resulting magnetic field magnitude measured at 100 km altitude above the distribution shown in panel d). Panel f) plots radial profiles of the circumferentially averaged magnetic field magnitude at 4 altitudes (50, 100, 200, 400 km) with standard deviations shown as shaded regions. Panel g) shows normalized versions of the same curves as in panel f).

Figure 3: Dependence of $|B|_{ave}$ on magnetization polar angle. Panel a) shows normalized $|B|_{ave}$ as a function of the polar angle of the magnetization axis at 185 km and 400 km for 5 horizontal coherence wavelengths. Panel b) shows radial magnetic field profiles at 185 km and 400 km altitude over demagnetized craters of three different diameters and polar angles (0°, 45°, 90°) where the horizontal coherence wavelength is 512 km.

Figure 4: dependence of $|B|_{ave}$ on the vertical coherence wavelength of magnetization. Panel a) shows $|B|_{ave}$ as a function of vertical coherence wavelength at 185 km at 400 km for three horizontal coherence wavelengths. Panel b) normalized radial profiles of $|B|_{ave}$ measured over a 500 km-diameter crater for five vertical coherence wavelengths.

Figure 5: $|B|_{ave}$ (abscissa) is plotted versus altitude (ordinate) for three different horizontal and vertical coherence wavelengths and an RMS magnetization strength of 30 A/m. Green diamonds represent the 50th and 90th percentiles of the global MAG and ER magnetic maps at 400 km and 185 km respectively.

Figure 6: panels a) and b) show peak pressure contours in 2 dimensions resulting from the CTH hydrocode simulation [McGlaun et al., 1990] of a 250 km-diameter spherical impactor of density

3000 kg/m^3, striking a layered Mars vertically at 9 km/s [Louzada and Stewart, 2009]. Panel c) plots the saturation remanence of pyrrhotite as a function of static pressure from Rochette et al. [2003]. Panel d) combines the results in panels b) and c) to plot the fractional remaining magnetization as a function of depth and radius from the impact point. The upper 5 km of crust here is assumed not to be coherently magnetized due to impact gardening and so can be ignored in panel d). The abscissa axis in panels b) and d) is distance from the impact point, along a great circle.

Figure 7: Magnetic field magnitude is plotted at three different altitudes (100 km, 185 km and 400 km) above random magnetization distributions with a horizontal coherence wavelength of 512 km, a vertical coherence wavelength of 24 km and RMS magnetization of 10 A/m, into which have been placed circular demagnetized zones with diameters of 300 km, 400 km, 550 km, 750 km at 1000 km. For each crater, the demagnetization 'round-up' zone is equal to 25% of the diameter (e.g. for the '1000 km crater', the magnetization is zero out to a radius of 375 km, then increases linearly to a radius of 625 km.)

Figure 8: the variable $B_{<0.5R}/B_{1.5\text{-}2R}$ (the ratio of magnetic field inside 0.5 basin radii to that between 1.5 and 2 basin radii) is plotted as a function of altitude, coherence wavelength and demagnetization diameter. Panels a) - c) plot this ratio as a function of altitude for five crater diameters (300 km, 400 km, 550 km, 750 km, 1000 km) and 3 coherence wavelengths (256 km, 512 km, 1024 km). Panels d) and e) plot the same ratio as a function of demagnetization diameter and horizontal coherence wavelength for our 2 observation altitudes: 185 km and 400 km.

Figure 9-13: Demagnetization fitting results for (in order) the Isidis, Argyre, Hellas, Utopia and North Polar basins. Panels a) and b) show magnetic field magnitude at 185 km and 400 km respectively. Note the color scale is logarithmic and the colors are draped over shaded MOLA 1/16° topography [Smith et al., 2001]. The white rings represent the inner and outer topographic boundaries as defined by Frey [2006, 2008]. The red ring represents the demagnetization diameter of the χ^2 minimum. The 3 magenta rings represent the center and full width half max values of the distribution of demagnetization diameter inside the 1-sigma confidence interval (shown in panel l). The white dotted radial lines show the azimuth range over which radial profiles of B_{185} and B_{400} are averaged (values also given in table 1). These profiles are shown as black lines in panel c), over which the best-fit model predictions are plotted with pink and green dashed lines respectively. Panel d) shows a histogram of the distribution of values of horizontal coherence wavelength within the 1-sigma confidence interval. Panels e) through l) are arranged symmetrically, with demagnetization gradient width as the abscissa in the left column, magnetization strength in the middle column and demagnetization radius in the right column and horizontal coherence wavelength as the ordinate in the middle row. Panels e) through h) show four different two-dimensional slices of the 4-dimensional χ^2 space defined by demagnetization radius, demagnetization gradient width, magnetization strength and horizontal coherence wavelength. Each 2-d slice correspondents to the χ^2 minimum in the other two dimensions. The white contour corresponds to the 1-sigma confidence interval (i.e. where χ^2 is less than 1.0+min (χ^2)). The yellow contour represents where $\chi^2 < 0.5$ +min (χ^2). The latter contour is not always visible because nearest-neighbor smoothing his applied over each slice for display purposes. Panels j) through l) plot histograms of the distributions of demagnetization gradient,

magnetization strength and demagnetization radius inside the 1-sigma confidence interval. Gaussian curves (solid red/purple lines) are fit to the distributions of magnetization strength and demagnetization radius in panels k) and l) respectively for the purposes of determining center and FWHM values (given in table 1).

Figure 14: Comparison of magnetization-versus-radius curves. Shown in pink and blue are curves derived from the present work for Argyre and Hellas, respectively for all values of demagnetization gradient width contained in the 1-sigma confidence interval (see panel j of figures 9-13) between 0 km and 1100 km. The solid black line is the peak shock pressure as a function of radius averaged over the depth interval 10 km-60 km depth from a CTH hydrocode impact simulation (shown in 2 dimensions in figure 6b). The dotted orange line plots the remaining magnetization as a function of radius calculated using the peak pressure (solid black line) and the pressure-demagnetization curve from Rochette et al. [2003] shown in figure 6c.

Figure 15: Comparison of 400 km altitude evaluations of the internal dipole model of Langlais, Purucker and Mandea (LPM) [Langlais et al., 2004] and the correlative model used in the present work. The color scale is highly nonuniform and emphasizes differences between small values of magnetic field magnitude. The contribution from non-crustal sources varies geographically and ranges from 3 nT to 5 nT in the LPM model and from 1.0 nT to 2.5 nT in the correlative model.

Figure 16: The average error ΔB_{400} (equation 3) is plotted as a function of B_{400} for 3 different values of B_{ext}, with the assumption that $\Delta B_{cal} = 0.5$ nT.

Tables:

Basin name	Isidis	Argyre	Hellas	Utopia	N.Polar
Latitude of basin center[1]	13.4° N	49.0° S	42.3° S	45.0° N	80.0° N
East Longitude of basin center[1]	87.8°	317.5°	66.4°	115.5°	195.2°
Hartman and Neukum [2001] model age (Gyr)[1]	3.81	4.04	4.07	4.11	4.12
Topographic ring diameters[1] (km)	1048 1352 1845	905 1315 2350	2070 3085	2360 3380 4210	1486 2145
Angular range considered for magnetic modeling (0° is east from center of basin)	90-60 (330°)	50-175 (125°)	340-160 (180°)	80-285 (205°)	60-120 (60°)
Demagnetization diameter (km): Gaussian fit inside 1-sigma confidence interval (center - HWHM, **Center**, Center + HWHM)	1298 **1573** 1764	1572 **1882** 2111	2442 **2605** 2679	2845 **3121** 3410	1681 **2089** 2466
Ratio: Demagnetization/Inner topographic diameter	1.50	2.078	1.26	1.32	1.41
Ratio: Demagnetization/Outer topographic diameter	0.85	0.80	0.84	0.74	0.97
Mean best fit lateral coherence wavelength (km) (**mean**, standard deviation)	**1198** 217	**761** 225	**1152** 202	**788** 295	**650** 239
Best fits of demag. gradient width * (km) (**mean**, standard deviation)	**455** 325	**454** 354	**441** 283	**453** 336	**518** 361
Magnetization (A/m): Gaussian fit inside 1-sigma confidence interval (center - HWHM, **Center**, Center + HWHM)	0.71 **1.04** 1.37	1.58 **2.65** 4.39	1.59 **1.66** 1.93	0.46 **0.73** 1.30	2.09 **4.52** 8.88

Table 1: Physical properties and magnetic modeling/fitting results are given for the 5 large impact basins Isidis, Argyre, Hellas, Utopia and North Polar.

[1]Basin locations, model ages and topographic ring diameters are taken from Frey [2008]. Model ages are not referenced in the text, but shown for completeness.

*Distributions of demagnetization gradient width generally span the entire explored range from 0 km to 1100 km, so mean and standard deviation values are accompanied by this caveat.

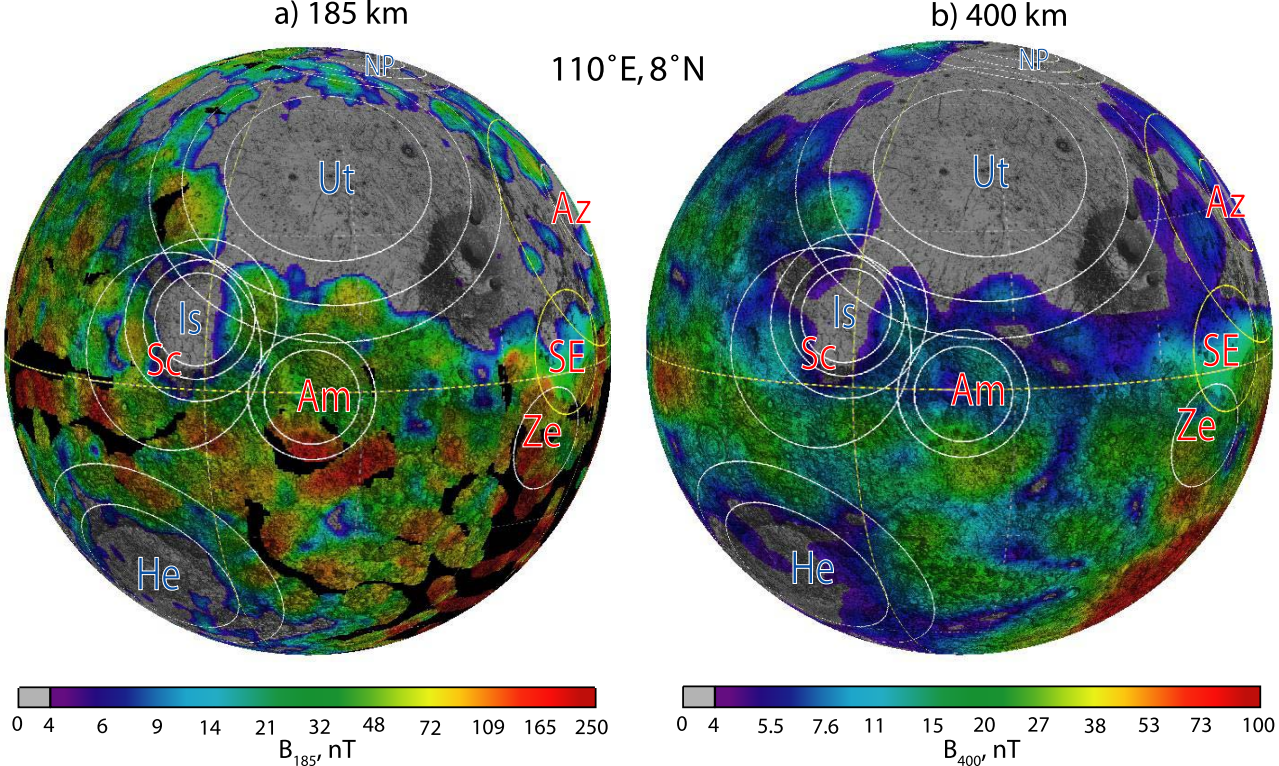
a) 185 km
b) 400 km
110˚E, 8˚N
NP
Ut
Az
Is
Sc
SE
Am
Ze
He
0 4 6 9 14 21 32 48 72 109 165 250
B185, nT
0 4 5.5 7.6 11 15 20 27 38 53 73 100
B400, nT

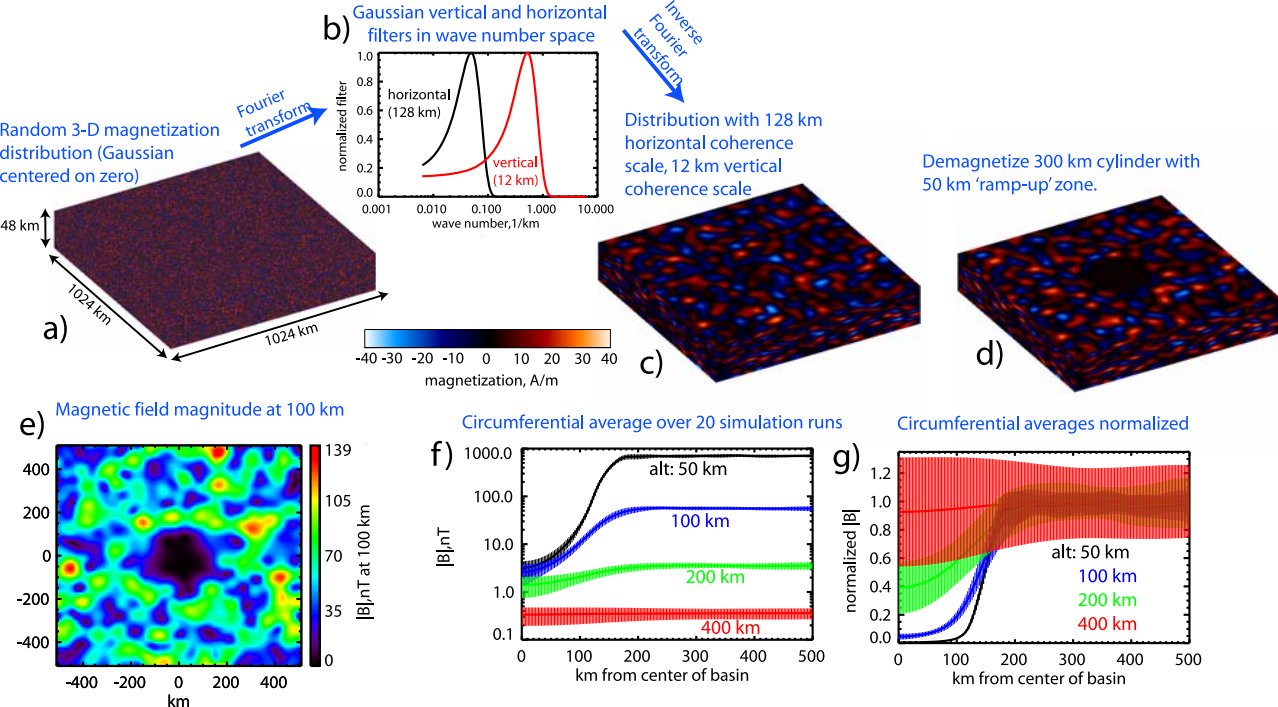
Random 3-D magnetization distribution (Gaussian centered on zero)
Fourier transform
b)
Gaussian vertical and horizontal filters in wave number space
horizontal (128 km)
vertical (12 km)
normalized filter
wave number,1/km
Inverse Fourier transform
Distribution with 128 km horizontal coherence scale, 12 km vertical coherence scale
Demagnetize 300 km cylinder with 50 km 'ramp-up' zone.
48 km
1024 km
1024 km
a)
-40 -30 -20 -10 0 10 20 30 40
magnetization, A/m
c)
d)
e)
Magnetic field magnitude at 100 km
|B|,nT at 100 km
km
f)
Circumferential average over 20 simulation runs
alt: 50 km
100 km
200 km
400 km
|B|,nT
km from center of basin
g)
Circumferential averages normalized
normalized |B|
km from center of basin

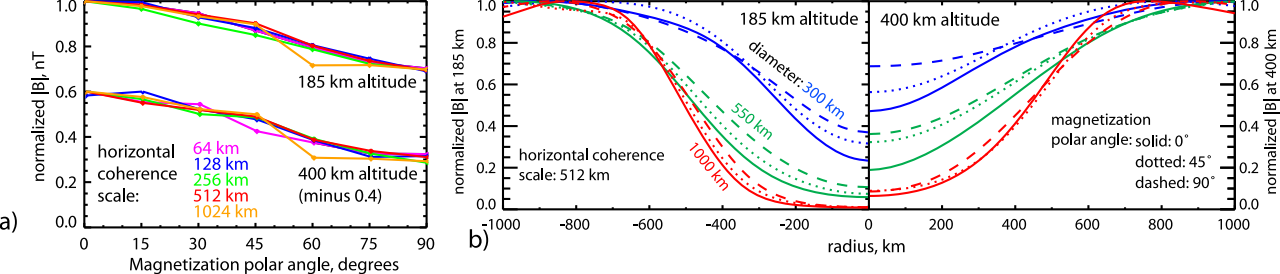
a)
normalized |B|, nT
185 km altitude
400 km altitude
(minus 0.4)
horizontal
coherence
scale:
64 km
128 km
256 km
512 km
1024 km
Magnetization polar angle, degrees
b)
normalized |B| at 185 km
185 km altitude
diameter: 300 km
550 km
1000 km
horizontal coherence
scale: 512 km
normalized |B| at 400 km
400 km altitude
magnetization
polar angle: solid: 0˚
dotted: 45˚
dashed: 90˚
radius, km

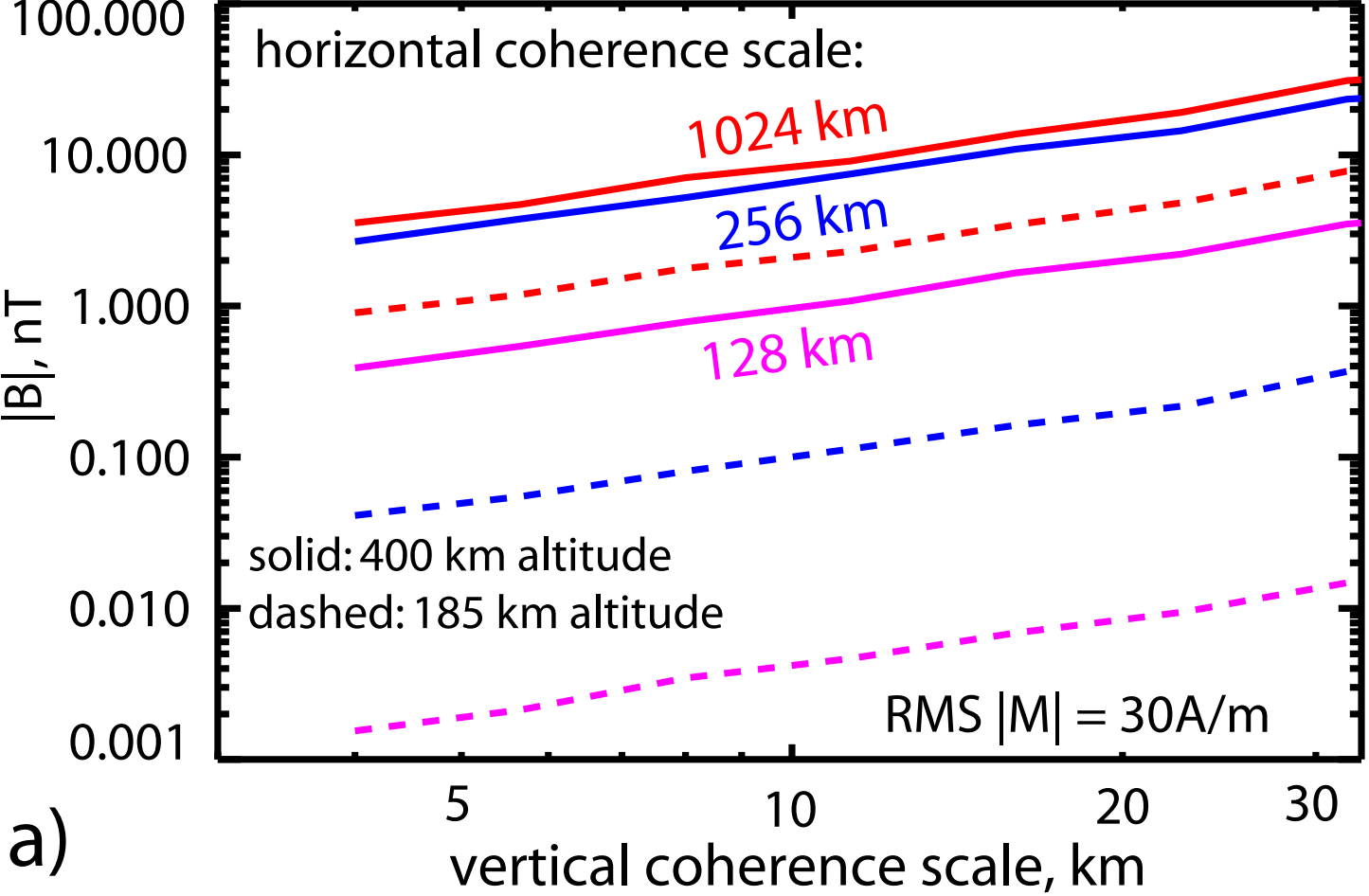
horizontal coherence scale:
1024 km
256 km
128 km
solid: 400 km altitude
dashed: 185 km altitude
RMS |M| = 30A/m
|B|, nT
100.000
10.000
1.000
0.100
0.010
0.001
5
10
20
30
vertical coherence scale, km

a)

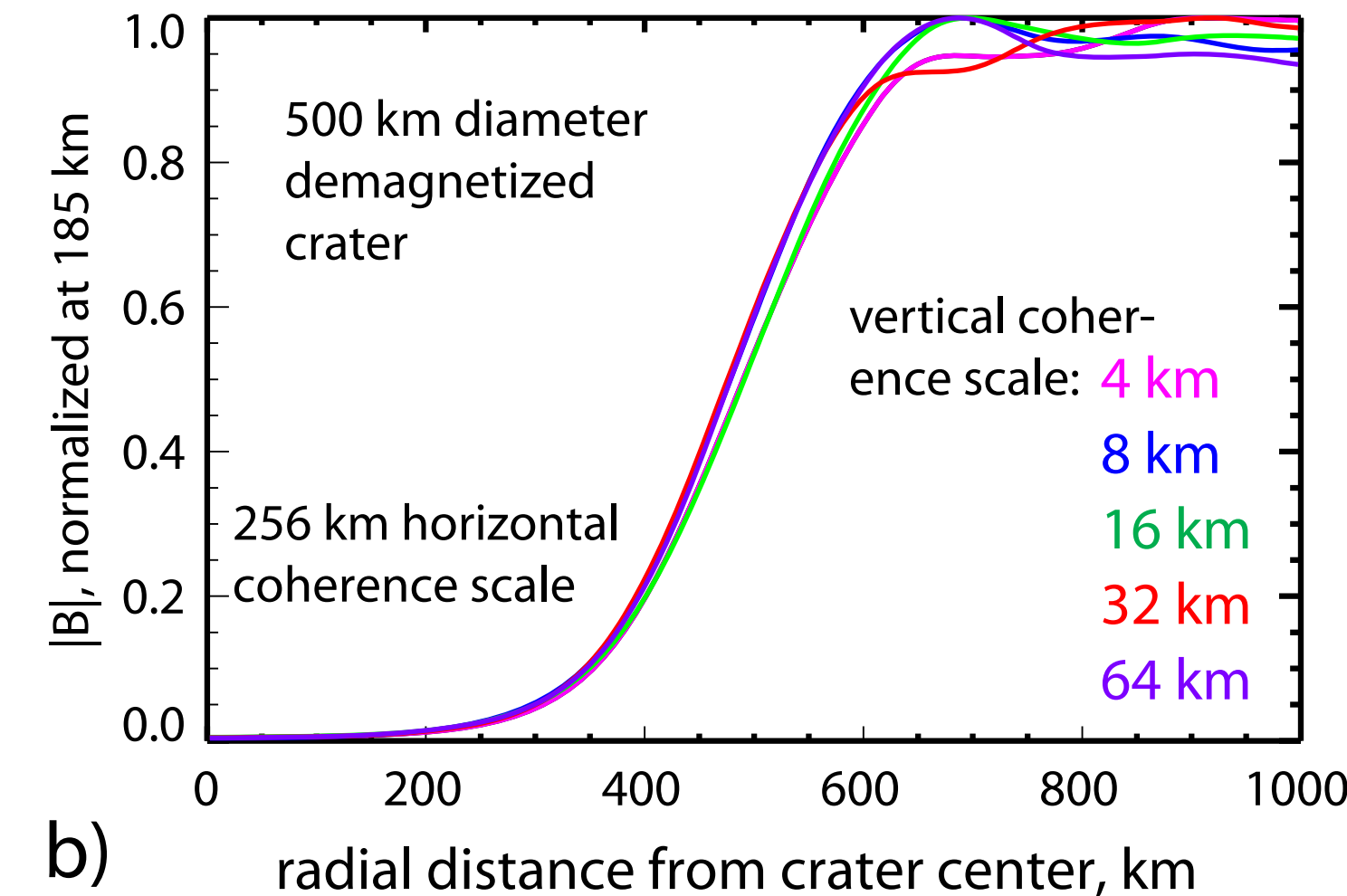
500 km diameter
demagnetized
crater
256 km horizontal
coherence scale
vertical coher-
ence scale: 4 km
8 km
16 km
32 km
64 km
|B|, normalized at 185 km
1.0
0.8
0.6
0.4
0.2
0.0
0
200
400
600
800
1000
radial distance from crater center, km

b)

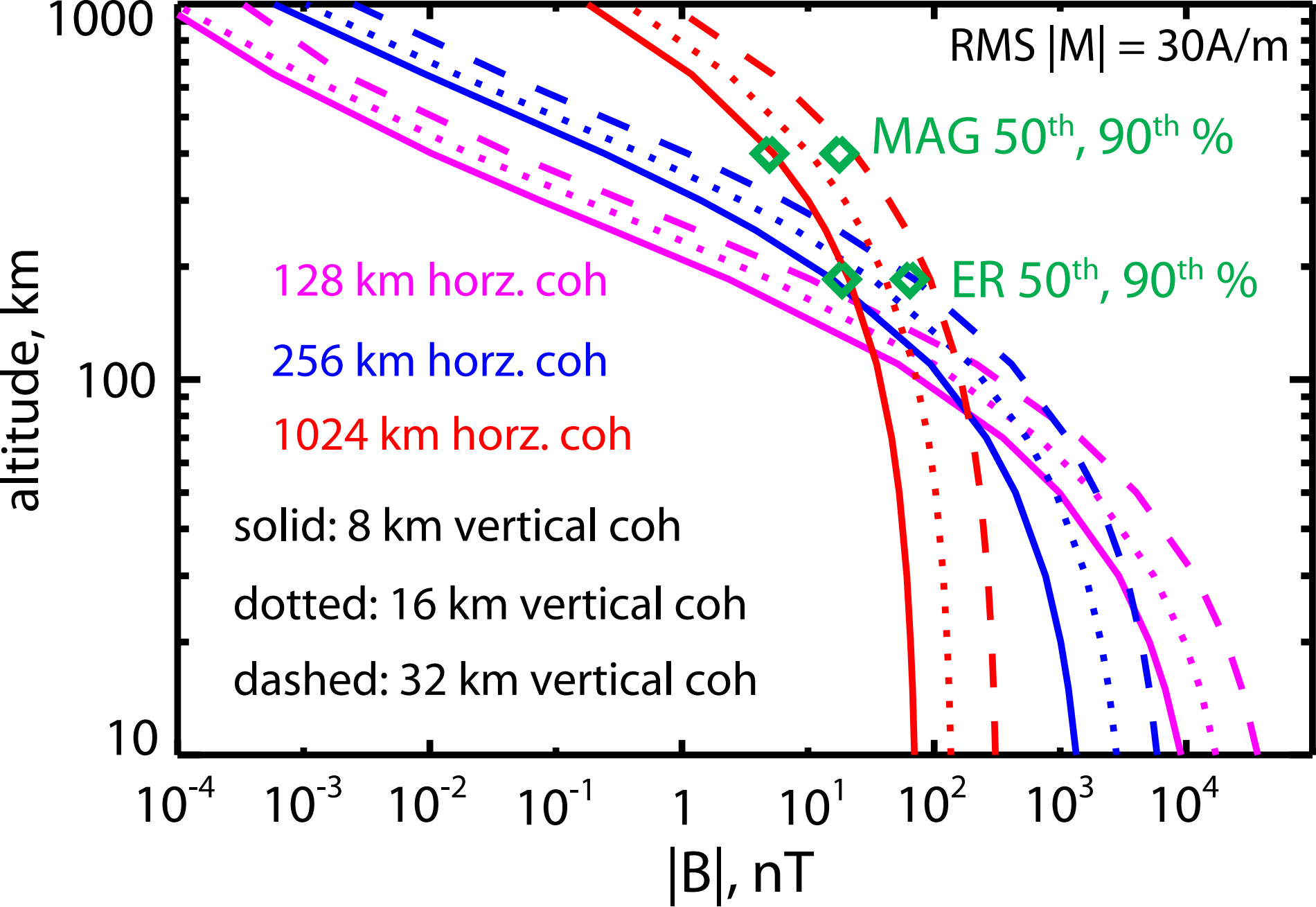
RMS |M| = 30A/m
MAG 50th, 90th %
ER 50th, 90th %
128 km horz. coh
256 km horz. coh
1024 km horz. coh
solid: 8 km vertical coh
dotted: 16 km vertical coh
dashed: 32 km vertical coh
altitude, km
1000
100
10
10-4
10-3
10-2
10-1
1
101
102
103
104
|B|, nT

CTH hydrocode impact simulation. 250 km diameter impactor, 9 km/s, vertical

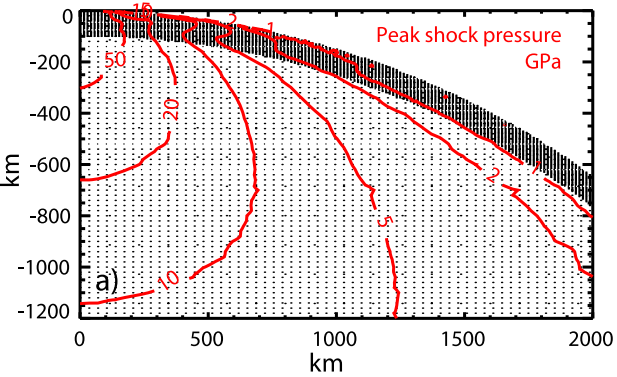

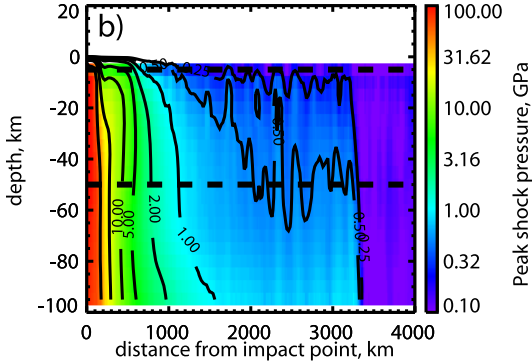

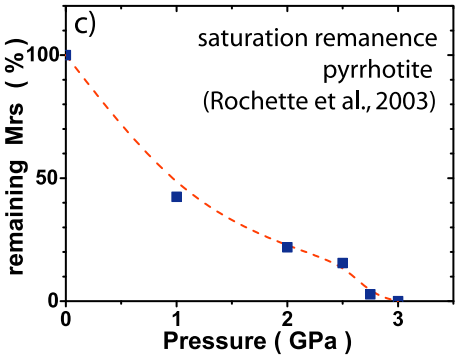

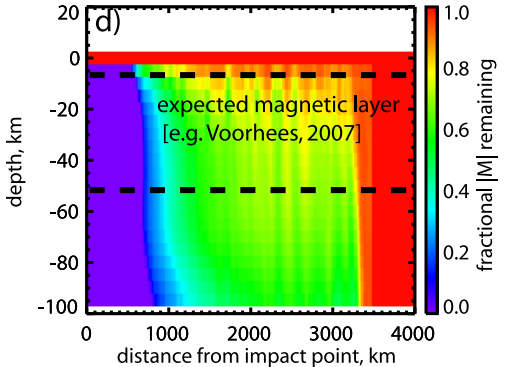

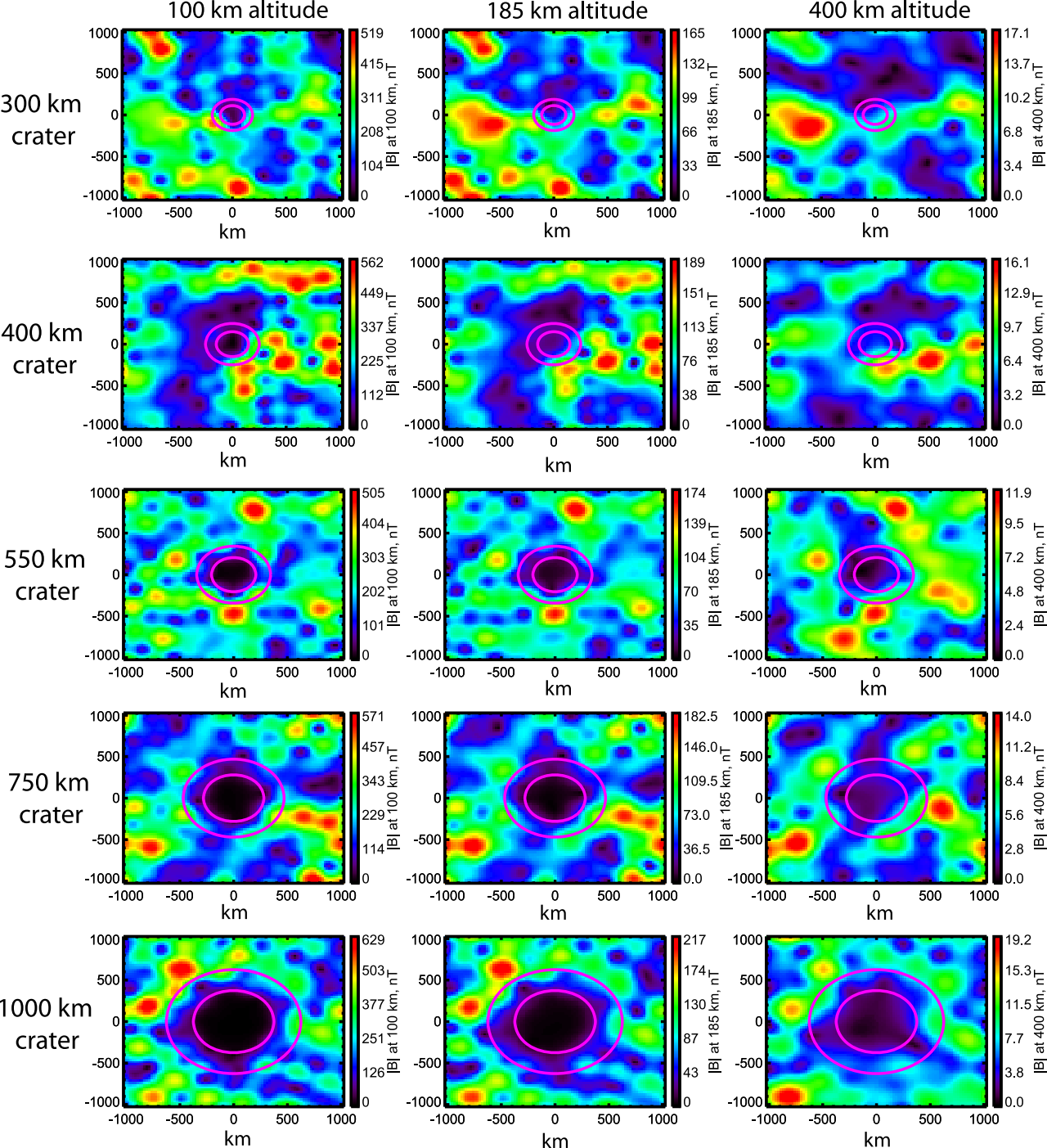
100 km altitude
185 km altitude
400 km altitude
300 km crater
400 km crater
550 km crater
750 km crater
1000 km crater
km
|B| at 100 km, nT
|B| at 185 km, nT
|B| at 400 km, nT

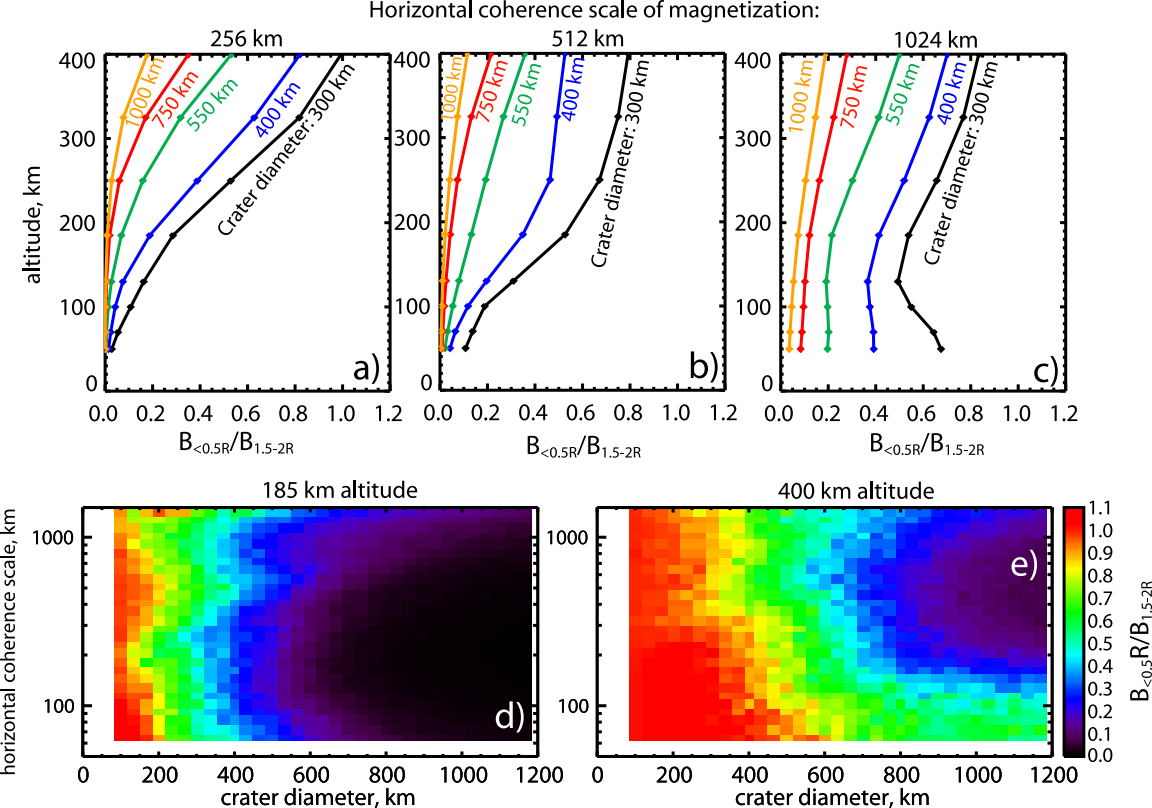
Horizontal coherence scale of magnetization:
256 km
512 km
1024 km
altitude, km
1000 km
750 km
550 km
400 km
Crater diameter: 300 km
a)
b)
c)
$B_{<0.5R}/B_{1.5\text{-}2R}$
185 km altitude
400 km altitude
horizontal coherence scale, km
crater diameter, km
d)
e)
$B_{<0.5}R/B_{1.5\text{-}2R}$

Isidis Basin

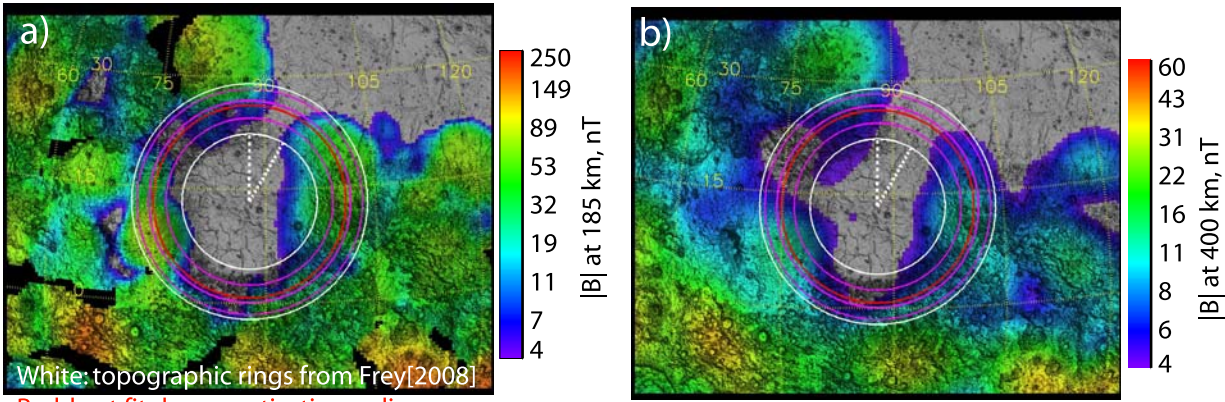

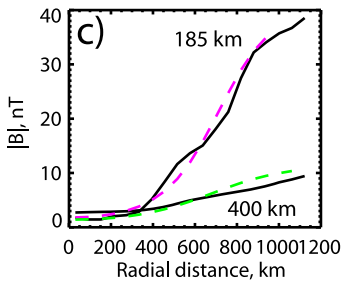

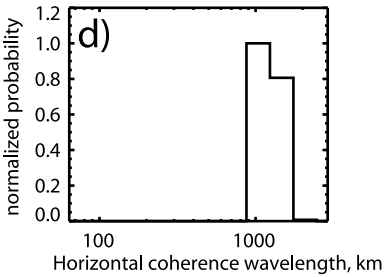

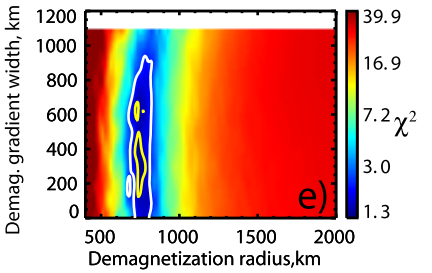

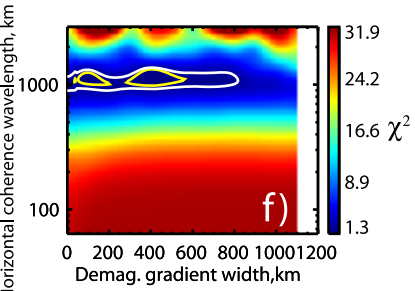

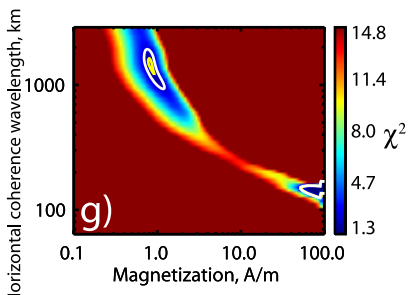

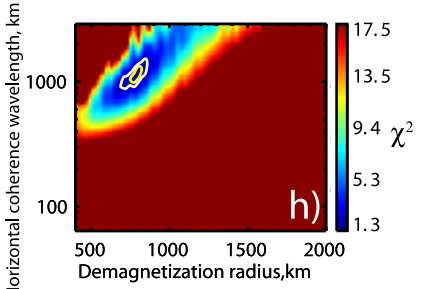

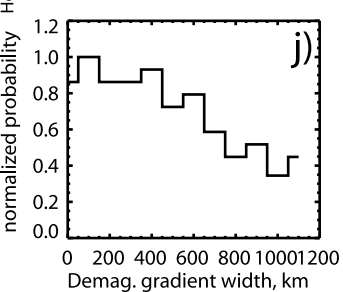

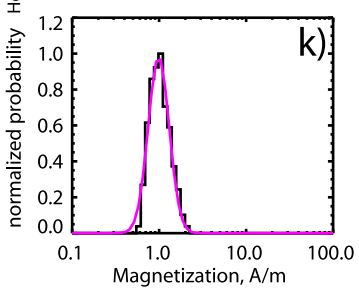

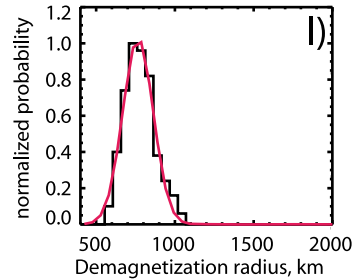

Argyre Basin

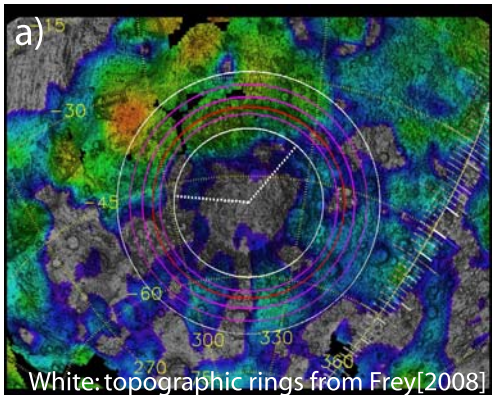

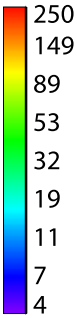

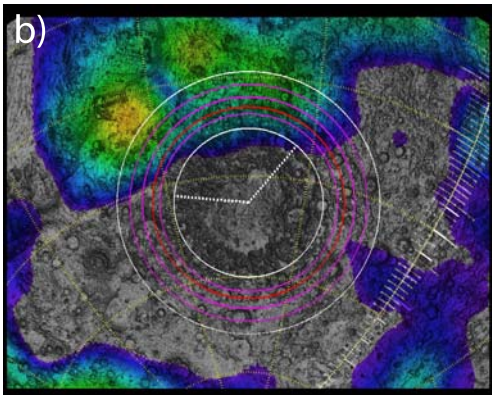

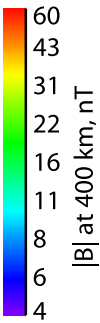

Red: best fit demagnetization radius

Magenta: Center & FWHM of demag. radius in 1-σ confidence interval (panel l)

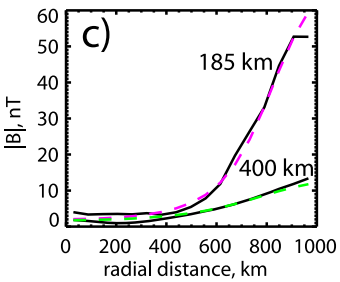

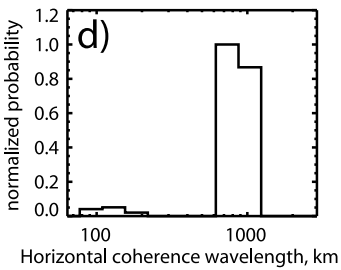

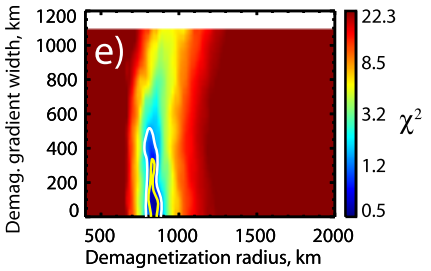

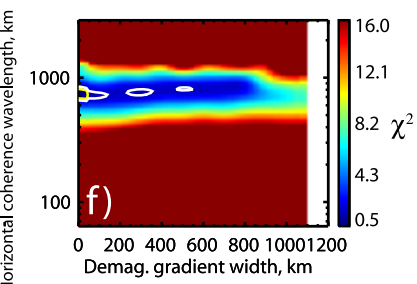

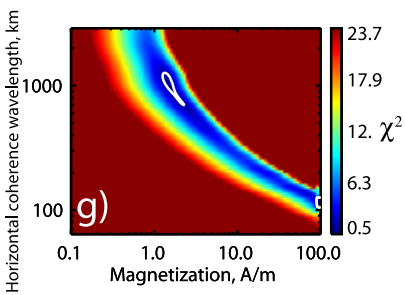

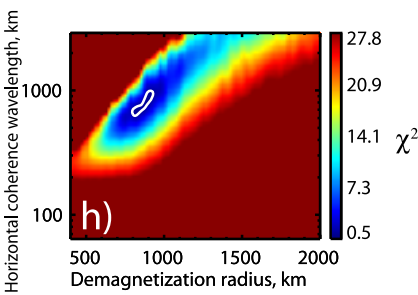

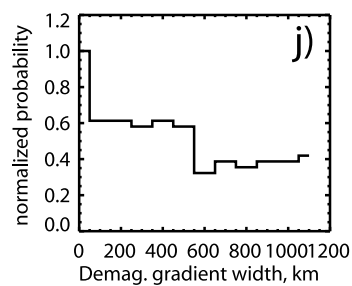

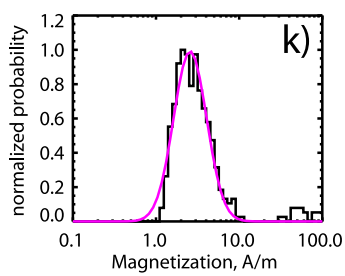

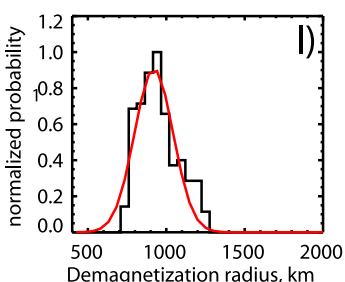

Hellas Basin

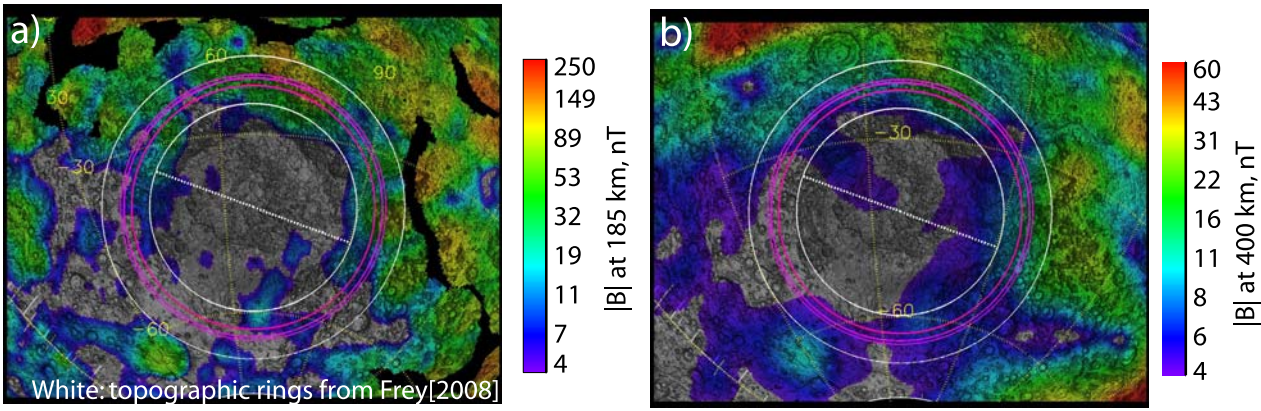

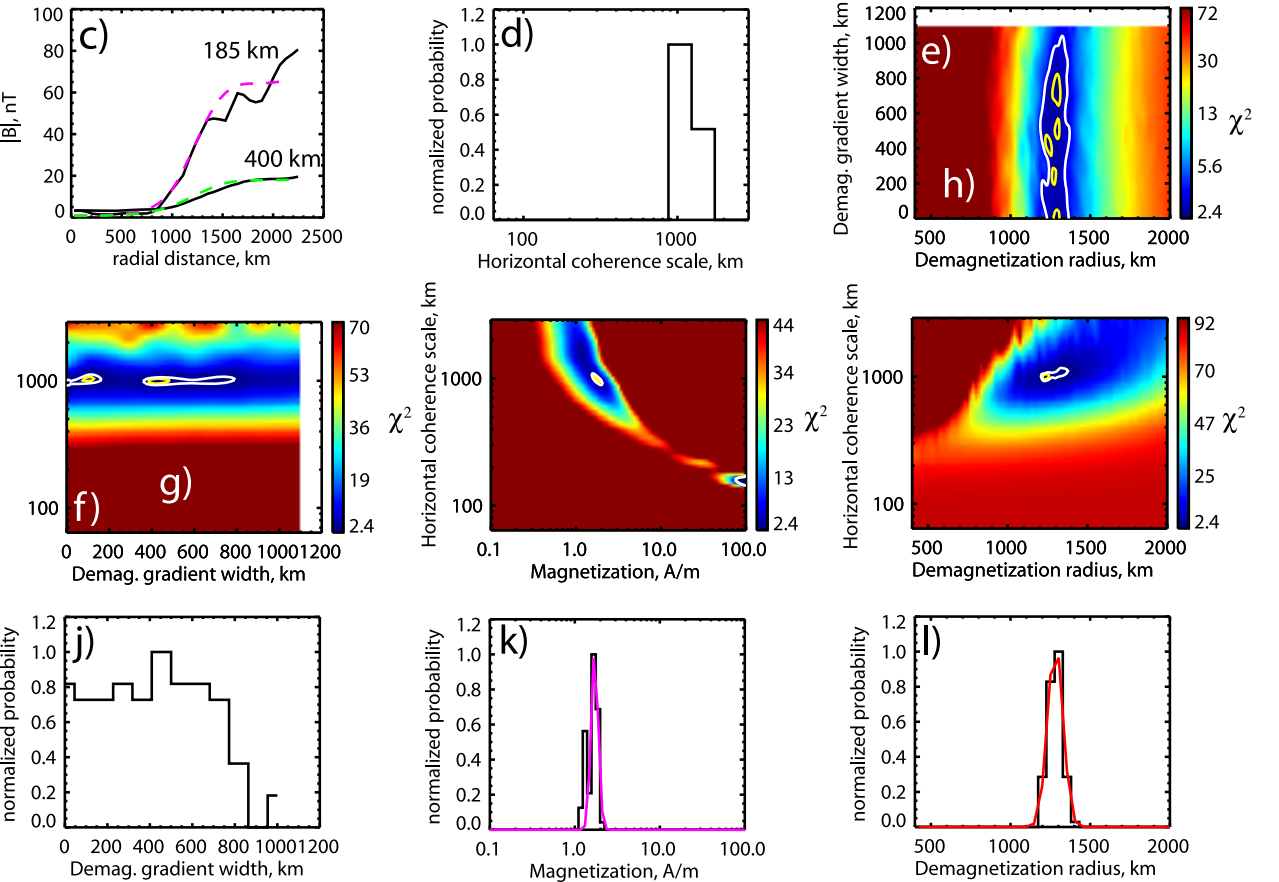

Utopia Basin

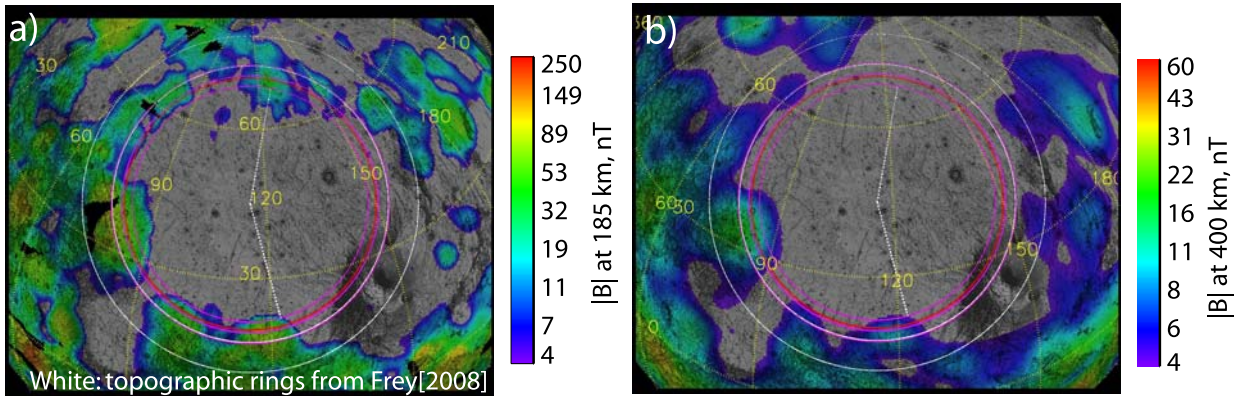

Red: best fit demagnetization radius

Magenta: Center & FWHM of demag. radius in 1-σ confidence interval (panel l)

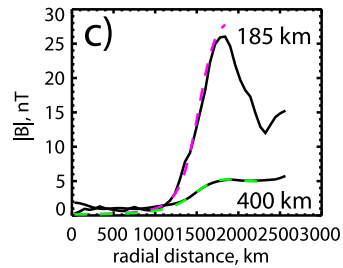

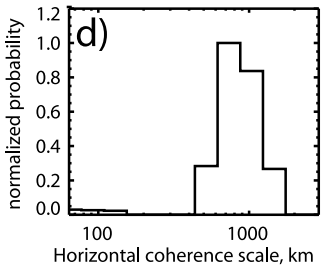

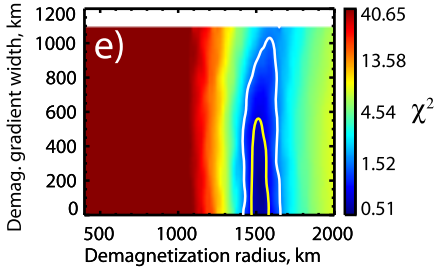

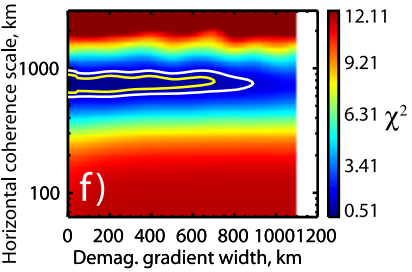

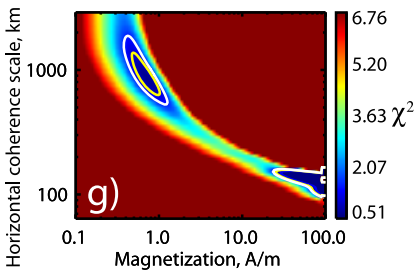

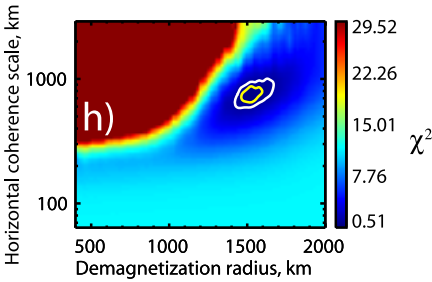

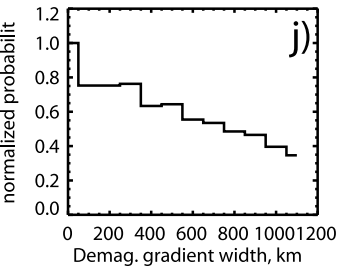

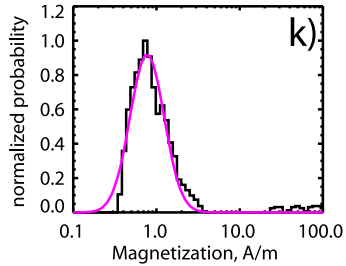

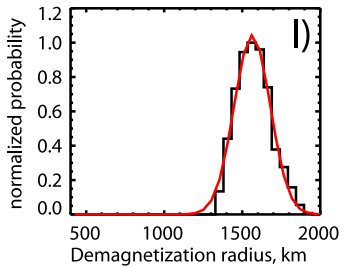

North Polar Basin

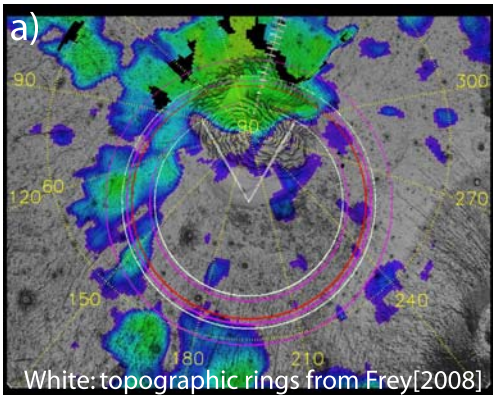

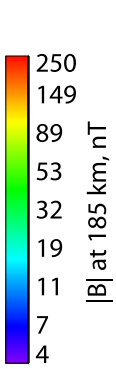

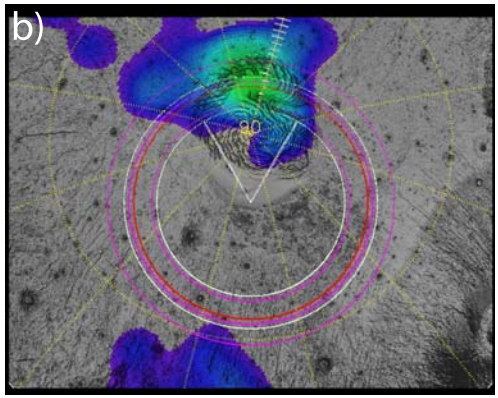

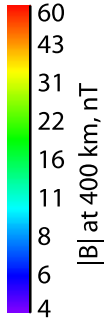

Red: best fit demagnetization radius

Magenta: Center & FWHM of demag. radius in 1-σ confidence interval (panel l)

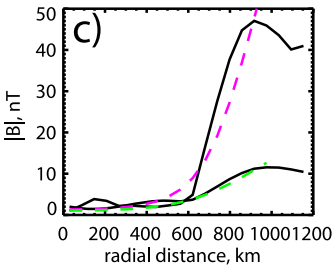

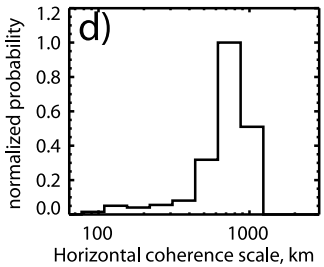

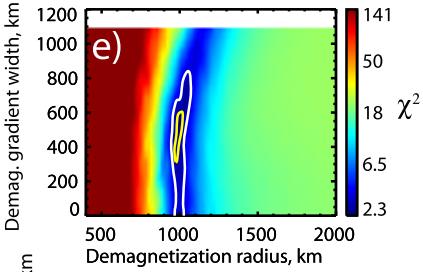

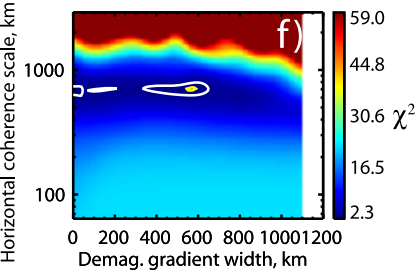

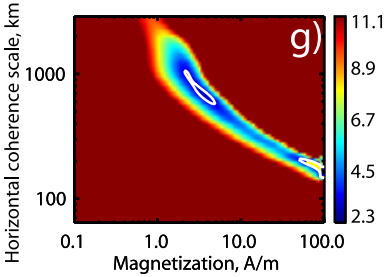

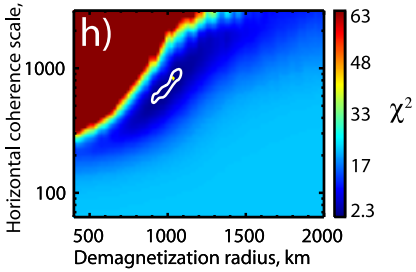

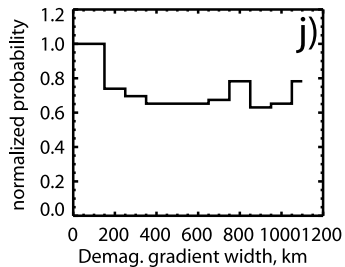

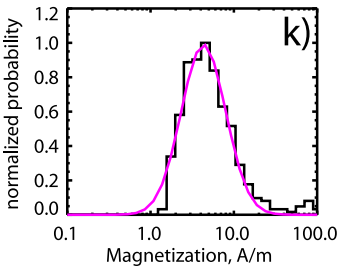

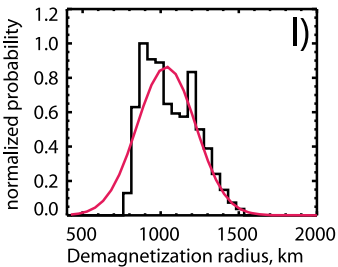

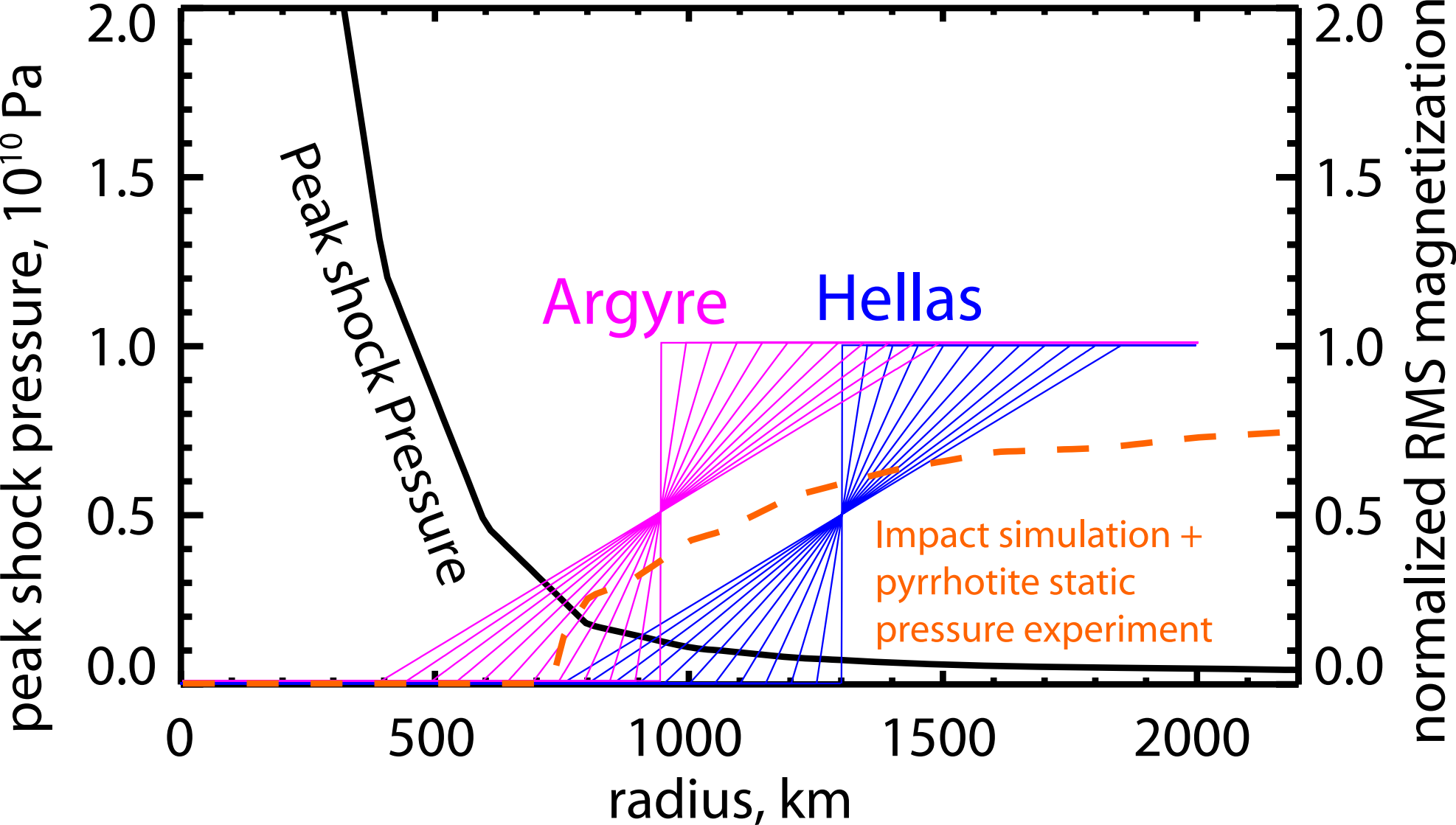
peak shock pressure, 10^{10} Pa
normalized RMS magnetization
radius, km
Peak shock Pressure
Argyre
Hellas
Impact simulation +
pyrrhotite static
pressure experiment
0.0
0.5
1.0
1.5
2.0
0
500
1000
1500
2000

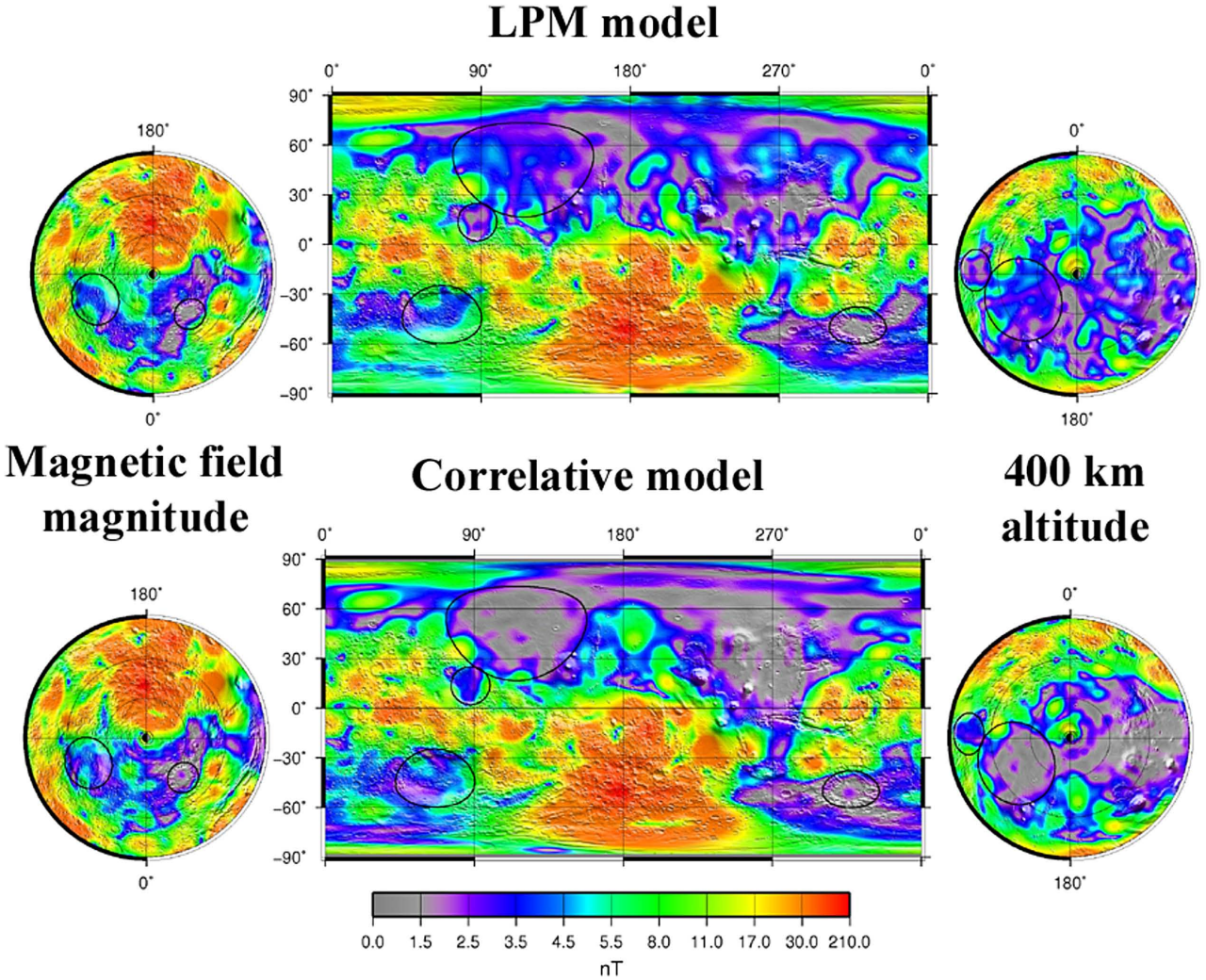
LPM model
Magnetic field magnitude
Correlative model
400 km altitude
0°
90°
180°
270°
60°
30°
-30°
-60°
-90°
0.0
1.5
2.5
3.5
4.5
5.5
8.0
11.0
17.0
30.0
210.0
nT

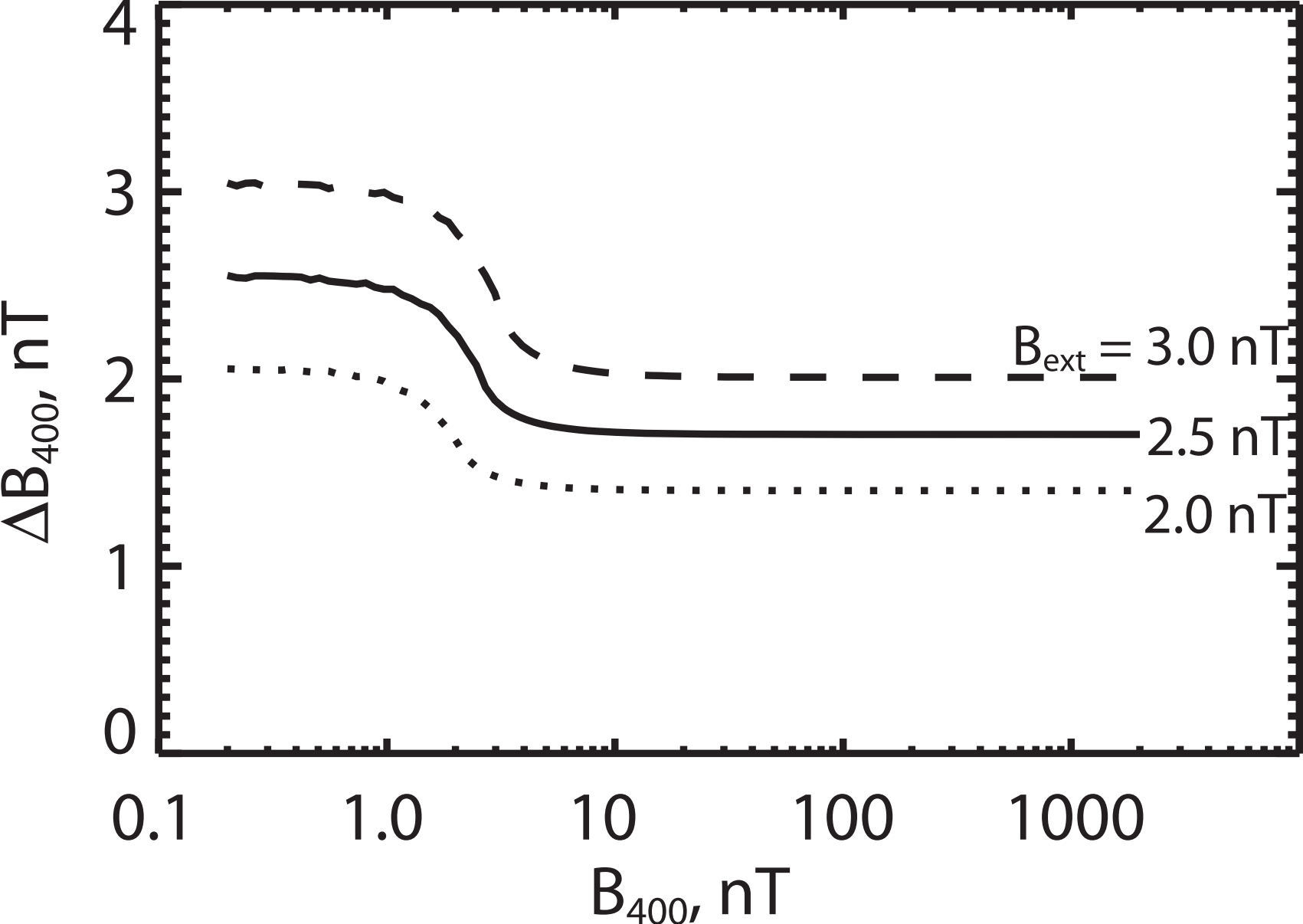
4
3
2
1
0
ΔB400, nT
Bext = 3.0 nT
2.5 nT
2.0 nT
0.1
1.0
10
100
1000
B400, nT